Article

DGKB mediates radioresistance by regulating DGAT1-dependent lipotoxicity in glioblastoma

Graphical abstract

DGKB: Diacylglycerol kinase B; **DGAT1**: Diacylglycerol O-Acyltransferase 1; **DAG**: Diacylglycerol; **TG**: Triglyceride; **LDs**: Lipid droplets; **PA**: Phosphatidic acid
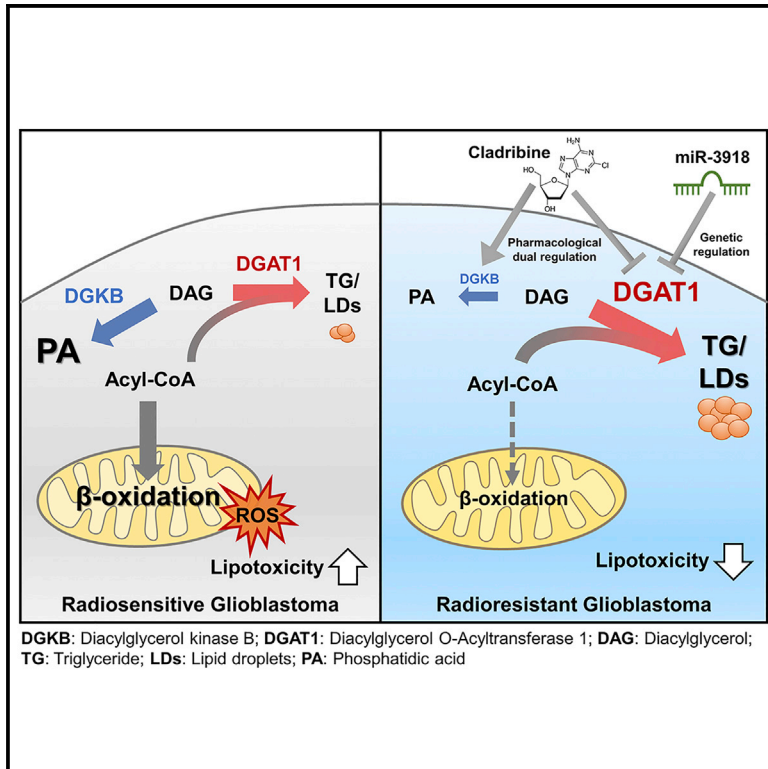
Authors

Hyunkoo Kang, Haksoo Lee, Kyeongmin Kim, ..., Jae-Myung Lee, HyeSook Youn, BuHyun Youn

Correspondence

bhyoun72@pusan.ac.kr

In brief

Kang et al. report that radioresistant GBM cells that express low levels of DGKB and high levels of DGAT1 prefer to store FAs in TG instead of utilizing them as an energy source to reduce mitochondrial ROS. Pharmacological or genetic regulation of DGKB and DGAT1 sensitizes GBM cells to radiotherapy.

Highlights

- Radioresistant GBM cells express low levels of DGKB and high levels of DGAT1

- DAG accumulation resulting from downregulated DGKB contributes to GBM radioresistance

- Upregulated DGAT1 confers radioresistance by decreasing FA oxidation

- Pharmacological or genetic regulation of DGKB and DGAT1 overcomes GBM radioresistance

CellPress

Article

DGKB mediates radioresistance by regulating DGAT1-dependent lipotoxicity in glioblastoma

Hyunkoo Kang,[1,9] Haksoo Lee,[1,9] Kyeongmin Kim,[2] Eunguk Shin,[1] Byeongsoo Kim,[1] JiHoon Kang,[3] Bohkyung Kim,[4] Jung Sub Lee,[5] Jae-Myung Lee,[6] HyeSook Youn,[7] and BuHyun Youn[1,8,10,*]

[1]Department of Integrated Biological Science, Pusan National University, Busan 46241, Republic of Korea
[2]Center Research Institute, Samjin Pharm. Co., Ltd, Seoul 07794, Republic of Korea
[3]Department of Hematology and Medical Oncology, Winship Cancer Institute of Emory, Emory University School of Medicine, Atlanta, GA 30322, USA
[4]Department of Food Science and Nutrition, Pusan National University, Busan 46241, Republic of Korea
[5]Department of Orthopaedic Surgery, Biomedical Research Institute, Pusan National University Hospital, Pusan National University School of Medicine, Busan 49241, Republic of Korea
[6]Department of Naval Architecture and Ocean Engineering, Pusan National University, Busan 46241, Republic of Korea
[7]Department of Integrative Bioscience and Biotechnology, Sejong University, Seoul 05006, Republic of Korea
[8]Department of Biological Sciences, Pusan National University, Busan 46241, Republic of Korea
[9]These authors contributed equally
[10]Lead contact
*Correspondence: bhyoun72@pusan.ac.kr
https://doi.org/10.1016/j.xcrm.2022.100880

SUMMARY

Glioblastoma (GBM) currently has a dismal prognosis. GBM cells that survive radiotherapy contribute to tumor progression and recurrence with metabolic advantages. Here, we show that diacylglycerol kinase B (DGKB), a regulator of the intracellular concentration of diacylglycerol (DAG), is significantly downregulated in radioresistant GBM cells. The downregulation of DGKB increases DAG accumulation and decreases fatty acid oxidation, contributing to radioresistance by reducing mitochondrial lipotoxicity. Diacylglycerol acyltransferase 1 (DGAT1), which catalyzes the formation of triglycerides from DAG, is increased after ionizing radiation. Genetic inhibition of DGAT1 using short hairpin RNA (shRNA) or microRNA-3918 (miR-3918) mimic suppresses radioresistance. We discover that cladribine, a clinical drug, activates DGKB, inhibits DGAT1, and sensitizes GBM cells to radiotherapy *in vitro* and *in vivo*. Together, our study demonstrates that DGKB downregulation and DGAT1 upregulation confer radioresistance by reducing mitochondrial lipotoxicity and suggests DGKB and DGAT1 as therapeutic targets to overcome GBM radioresistance.

INTRODUCTION

Glioblastoma (GBM) is the most prevalent and lethal primary tumor of the central nervous system (CNS). The median survival of GBM patients is only 15 months, which has not improved over the last two decades, and the 5-year recurrence rate of GBM after treatments is nearly 90%. The current standard of care for GBM patients is surgical resection followed by radiotherapy and temozolomide (TMZ). Notably, about 80% of GBM recurrences occur within radiation treatment fields.[1,2] In addition, GBM cells that survive radiotherapy become more aggressive and invasive. Therapeutic strategies to overcome the radioresistance are therefore urgently needed.

Recent studies report that altered metabolism, a hallmark of cancer, is closely associated with the radioresistance. Activations of glycolysis and its parallel pathway, the pentose phosphate pathway, promote the repair of ionizing radiation (IR)-induced DNA strand breaks and sustain rapid DNA metabolism, thereby minimizing the IR-induced cytotoxicity.[3] Glycolysis is highly activated by IR in GBM.[4,5] Likewise, mitochondrial

metabolism is tightly regulated to reduce oxidative damage.[6] Leveraging the altered metabolism might inform the development of novel therapeutics by enhancing the radiosensitivity of GBM.

Fatty acids (FAs) are major structural components of membrane phospholipids and are also used to produce ATP by mitochondria-mediated β-oxidation. Although glucose is a major fuel for most brain tumor cells, GBM cells acquire large amounts of FAs to promote cell growth, and inhibition of β-oxidation reduces their proliferation.[7] In addition, lipid droplets (LDs), the lipid storage organelles, are prevalent in GBM but undetectable in the normal brain, suggesting that lipid metabolism is also highly involved in GBM progression.[8,9] LDs are mainly composed of triglycerides (TGs), an ester derived from glycerol and three fatty acid molecules, and are known to play a role in maintaining lipid homeostasis. In a nutrient-poor condition, tumor cells quickly activate lipolysis to release FAs from LDs for structural lipid synthesis and energy production, facilitating tumor cell survival.[10,11] On the other hand, LDs also protect against excessive lipid catabolism by storing FAs in the form of TGs to avoid lipotoxicity
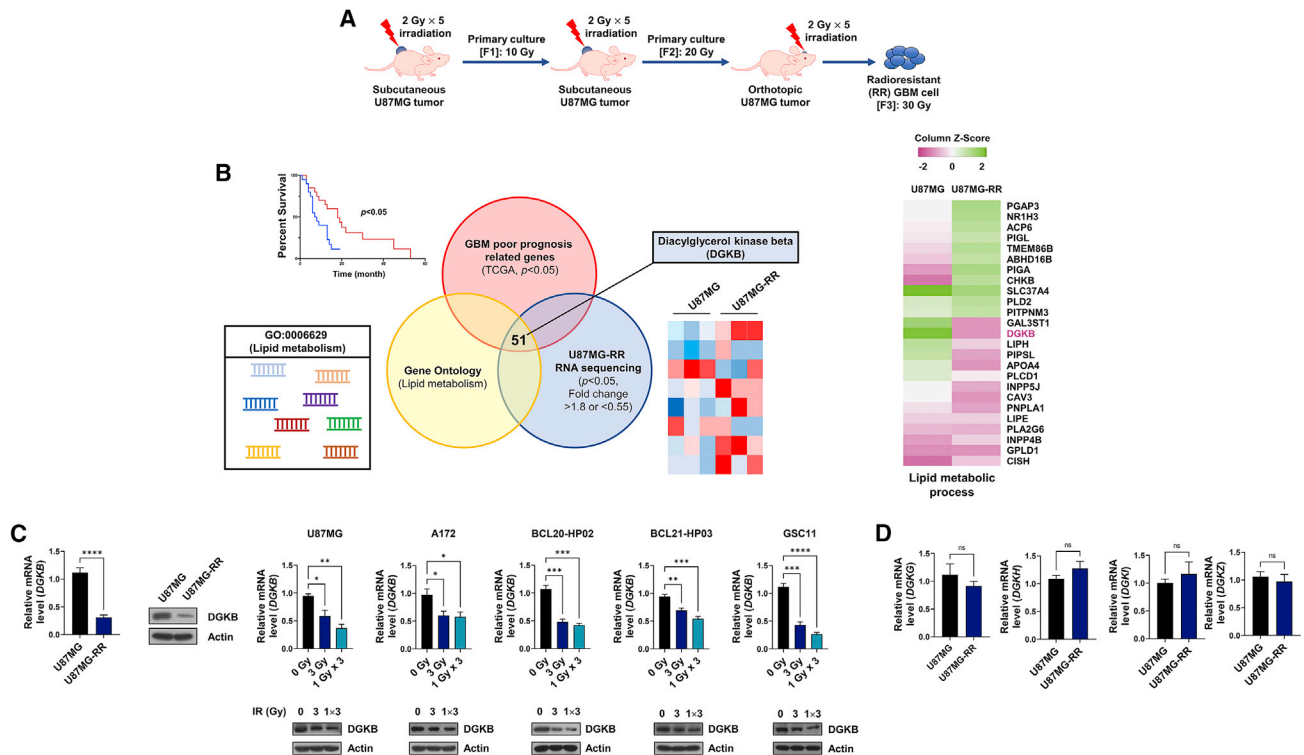
Figure 1. DGKB is downregulated in radioresistant GBM cells and radiation reduces DGKB expression

(A) A scheme illustrating the establishment of U87MG-RR cells through repeated xenograft and irradiation.

(B) Venn diagrams showing the number of genes overlapping among GBM poor-prognosis-related genes (TCGA, p < 0.05), lipid metabolism-associated genes (Gene Ontology [GO]: 0006629), and significantly differentially expressed genes from the RNA-sequencing analysis (p < 0.05, fold change >1.8 or <0.55) (left). The heatmap for the expression of genes in the term "lipid metabolism process" in U87MG-RR cells compared with parental cells (right).

(C) DGKB mRNA and protein levels in U87MG and U87MG-RR (left) as well as in U87MG, A172, BCL20-HP02, BCL21-HP03, and GSC11 without and with IR as indicated (right). Data are represented as mean ± SEM of three biological replicates.

(D) The mRNA level of DGK isoforms DGKG, DGKH, DGKI, and DGKZ in U87MG-RR and U87MG. Data are represented as mean ± SEM of three biological replicates. Statistical analysis was performed with one-way ANOVA plus a Dunnett's multiple comparisons test for (C) and Student's t test for (C) and (D). *p < 0.05, **p < 0.01, ***p < 0.001, ****p < 0.0001.

in cancer cells.[12–14] Because IR-induced reactive oxygen species (ROS) production renders cancer cells more sensitive to oxidative stress-induced cell damage, cellular processes that prevent lipotoxicity are essential for GBM maintenance.[15] Therefore, maintaining lipid homeostasis between FA oxidation and structural lipid synthesis is important for GBM growth and radioresistance.

Diacylglycerol kinases (DGKs) are a family of enzymes that catalyze the conversion of diacylglycerol (DAG) to phosphatidic acid (PA).[16] DGKs reduce the DAG level in the cell membrane, limiting DAG's functions as a secondary messenger and as a biosynthetic precursor of phospholipids and TGs. In the brain, most DGKs are abundantly expressed, with subtype-specific regional distribution.[17] Among 10 known DGK isozymes, diacylglycerol kinase B (DGKB) is mainly expressed in the cerebral cortex,[18] where GBM is predominantly located; however, the function of DGKB in GBM has rarely been studied. Diacylglycerol acyltransferase 1 (DGAT1), which catalyzes the esterification of acyl-coenzyme A (CoA) with diacylglycerol (DAG) to form TGs, is upregulated in GBM to reduce FA oxidation and protect against mitochondrial lipotoxicity by storing excess FAs into

TGs.[18] Since DGKB regulates the level of DAG, a substrate for TG, it might also play an important role in maintaining the lipid homeostasis and thereby regulates GBM growth.

In this study, we demonstrate that DGKB is significantly downregulated in radioresistant GBM cells, leading to DAG accumulation and thus preventing lipotoxicity. Activating DGKB or inhibiting IR-induced DGAT1 sensitizes GBM cells to radiotherapy by promoting FA catabolism and oxidative stress. Our study suggests a critical regulatory mechanism of lipid homeostasis and a strategy to overcome therapeutic resistance in GBM.

RESULTS

DGKB downregulation is associated with radioresistance in GBM cell lines and patient-derived glioblastoma stem-like cells

To explore factors contributing to radioresistance in GBM, we established radioresistant GBM cells using the human GBM cell line U87MG (Figure 1A). U87MG cells stably expressing luciferase were subcutaneously implanted in a BALB/c nude mouse

and exposed to IR (2 Gy/day for 5 days). *In vivo* bioluminescent imaging showed that the tumor markedly shrunk on day 14 after IR but regrew on day 21 after IR (Figure S1A, first cycle). Cells obtained from the tumor tissue that survived IR were again implanted subcutaneously in a BALB/c nude mouse and exposed to IR (2 Gy/day for 5 days). The tumor shrunk slightly on day 7 after IR but rapidly regrew (Figure S1A, second cycle). Tumor cells obtained from dissociating the tumor were orthotopically implanted in a BALB/c nude mouse and exposed to IR (2 Gy/day for 5 days). The tumor did not shrink by IR (Figure S1A, third cycle). Cells dissociated from the tumor were regarded as radioresistant U87MG cells (hereafter referred to as U87MG-RR cells).

We next assessed the radiosensitivity of U87MG and U87MG-RR cells after orthotopic xenograft in BALB/c nude mice. As shown in Figure S1B, the growth of U87MG-driven tumor was significantly inhibited by IR but that of U87MG-RR-driven tumor was hardly inhibited by IR. Furthermore, histological analysis showed that tumor infiltration was clearly increased in U87MG-RR xenografts compared with U87MG xenografts (Figure S1C). Because therapeutic resistance is closely related to cancer stemness, we analyzed stemness properties of U87MG and U87MG-RR cells in a serum-free stem cell medium. The mRNA levels of canonical stem cell transcription factors NANOG, OCT4, and SOX2 were significantly upregulated in U87MG-RR cells (Figure S1D). Moreover, limiting dilution assay showed that the frequency of glioblastoma stem-like cells (GSCs) capable of forming tumor spheres was remarkably high in U87MG-RR cells (Figure S1E). In sum, U87MG-RR cells not only were more resistant to IR but also were more invasive and had higher stem-like properties than their parental cells.

Next, we performed RNA-sequencing analysis of U87MG and U87MG-RR cells to find genes that might play a significant role in GBM radioresistance. Additionally, we analyzed GBM poor prognosis-associated genes using The Cancer Genome Atlas (TCGA) database and lipid metabolic process-associated genes using the Gene Ontology (GO) database (GO: 0006629). We identified 51 significantly differentially expressed genes overlapped with these three analyses (Figure 1B, left). Among them, we focused on DGKB, the major form of the DGK family in the brain (Figure 1B, right), and investigated the roles of DGKB in GBM radioresistance. Both mRNA and protein levels of DGKB were significantly lower in U87MG-RR cells compared with the control (Figure 1C, left). In addition, DGKB mRNA and protein levels were reduced in U87MG and A172 GBM cell lines and in BCL20-HP02, BCL21-HP03, and GSC11 patient-derived GSCs after treatment with a single fraction of 3 Gy or three fractions of 1 Gy (over a 24-h interval) (Figure 1C, right). On the other hand, mRNA levels of other DGK isoforms that expressed in the brain were similar in U87MG-RR and U87MG cells (Figure 1D).[19] DGKB SV3′ is an isoform of DGKB that lacks the C-terminal part encoded by the last exon, loses membrane localization, and has characteristics different from those of the full-length isoform (Figure S2A).[20,21] Because the expression of DGKB SV3′ barely changed in U87MG-RR or in the irradiated cells, only the full-length isoform of DGKB appeared to be involved in GBM radioresistance (Figure S2B). Collectively, these results demonstrate that IR-induced downregulation of DGKB may contribute to GBM radioresistance.

Downregulation of DGKB is important for radioresistant cancer cell proliferation and tumor growth

To examine the roles of DGKB in GBM cell proliferation and tumor growth, we established GBM cell lines with DGKB knockdown, knockout, or overexpression. DGKB overexpression reduced the cell viability and the colony-forming ability of irradiated U87MG-RR cells, whereas either knockdown or knockout of DGKB promoted the cell viability and the colony-forming ability of irradiated U87MG and the patient-derived GSCs (Figures 2A and 2B). Interestingly, the basic clonogenicity was unchanged between untreated control and DGKB knockdown or overexpression cells, suggesting that the effect of DGKB on GBM cell proliferation only plays a role under radiation (Figure 2B). To examine the role of DGKB *in vivo*, we established orthotopic xenograft mouse model using U87MG-RR cells with stable expression of luciferase. *In vivo* bioluminescent imaging showed that IR alone had minimal effect on the tumor growth, whereas IR combined with DGKB overexpression significantly reduced the tumor growth by 62.19% compared with IR alone (Figures 2C and 2D). H&E staining confirmed that the tumor size was remarkably decreased by combining IR with DGKB overexpression (Figure 2E). Immunohistochemistry (IHC) staining showed that the DGKB level was decreased by IR, and DGKB overexpression markedly enhanced IR-induced apoptosis, as determined by the level of cleaved caspase 3 (Figure 2F). Consequently, IR combined with DGKB overexpression conferred a significant survival benefit compared with untreated control (28 days of median survival) or IR alone (29 days of median survival) (Figure 2G). In summary, downregulated DGKB in GBM enhanced radioresistance by promoting cell proliferation and tumor growth.

Increased DAG, the substrate of DGKB, confers radioresistance to GBM cells

DGKB phosphorylates DAG to generate PA. To assess whether the role of DGKB in GBM radioresistance depended on its kinase activity, we generated a kinase-dead mutant (G495D) of DGKB that lacked the ability to convert DAG to PA (Figure 3A).[22] DGKB knockdown in U87MG-RR, U87MG, and patient-derived GSCs promoted cell viability after IR, which was abrogated by the ectopic expression of the wild-type but not mutant DGKB (Figure 3B). Because the enzymatic function of DGKB contributed to GBM cell survival, we focused on levels of the substrate and the product of DGKB. In U87MG-RR, U87MG, and patient-derived GSCs with DGKB knockdown, intracellular DAG levels were decreased, whereas PA levels were increased upon overexpressing wild-type but not mutant DGKB (Figures 3C and 3D). Next, we investigated whether increased DAG levels or decreased PA levels contributed to radioresistance by downregulated DGKB in GBM. Supplementation of DAG increased the cell viability in cells overexpressing DGKB, whereas PA supplementation did not affect the cell viability in DGKB knockdown cells after IR (Figure 3E). Furthermore, intracellular DAG levels in U87MG-RR cells are significantly higher than in U87MG cells, indicating that DAG accumulation is involved in GBM radioresistance (Figure 3F). Taken together, DAG accumulation resulting from downregulated DGKB contributes to GBM radioresistance.
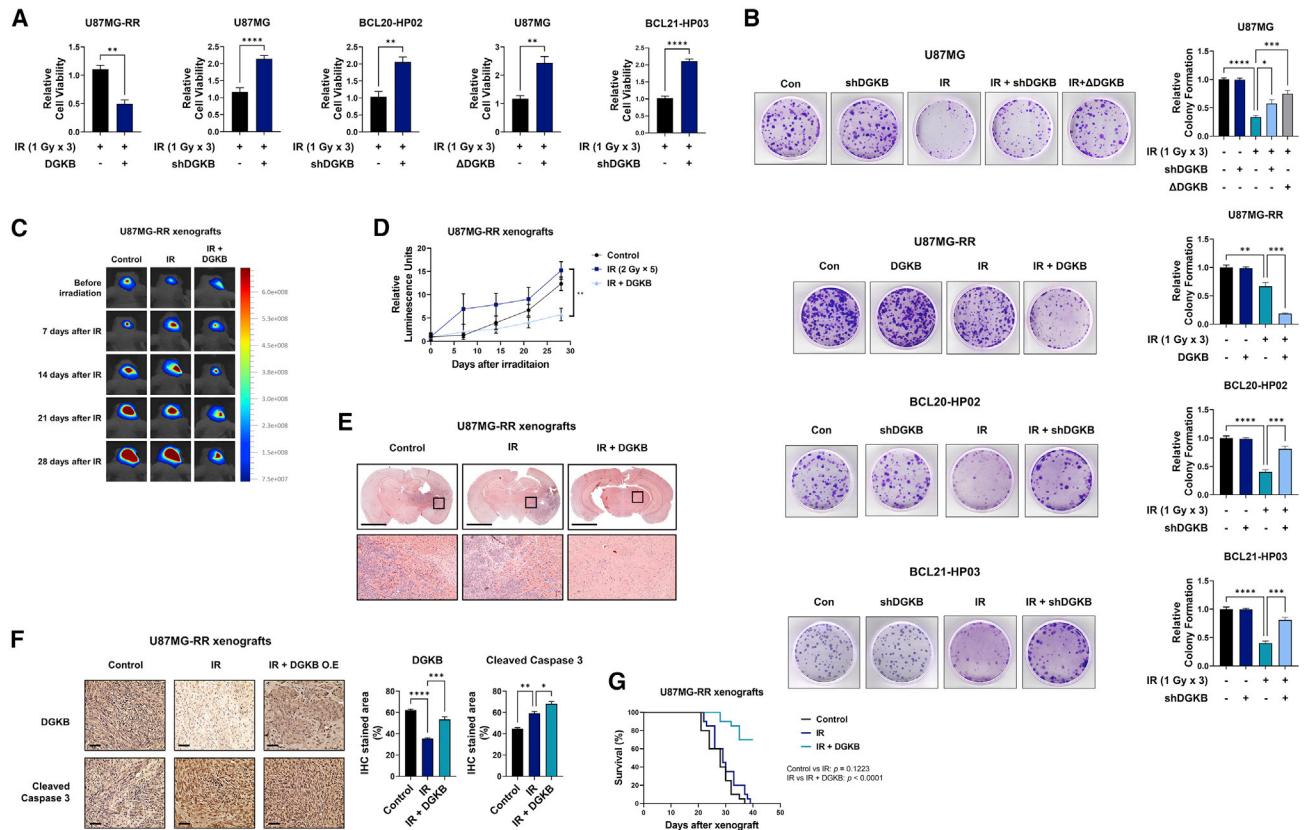
Figure 2. DGKB overexpression suppresses radioresistance and prolongs overall survival in GBM xenograft mouse models

(A) The changes in cell viability after IR or IR combined with DGKB overexpression in U87MG-RR, DGKB knockdown or knockout in U87MG, and DGKB knockdown in BCL20-HP02 and BCL21-HP03. Data are represented as mean ± SEM of three biological replicates.

(B) The changes in colony formation after shDGKB alone or DGKB overexpression alone, IR alone, or IR combined with DGKB overexpression in U87MG-RR, DGKB knockdown or knockout in U87MG, and DGKB knockdown in BCL20-HP02 and BCL21-HP03. Data are represented as mean ± SEM of three biological replicates.

(C and D) *In vivo* bioluminescence images (C) and relative luminescence units (D) of orthotopic xenografts derived from U87MG-RR in the untreated (control) group, IR group, and IR combined with DGKB overexpressing group (n = 20).

(E and F) Representative H&E staining (E) and IHC staining for DGKB and cleaved caspase 3 (F) of orthotopic xenograft GBM mouse models. Data are represented as mean ± SEM of three biological replicates. Scale bars, 2,000 μm (E) or 50 μm (F).

(G) Survival plots of mice with orthotopic xenograft GBM with DGKB overexpression and without (control) or with indicated treatment (IR treatments started 7 days after xenograft). Statistical analysis was performed with Student's t test for (A) one-way ANOVA plus a Tukey's multiple comparisons test for (B and D) compared with luminescence values of IR alone at 28 days after irradiation for (D), and Log rank (Mantel-Cox) test for (G). NS, non-significant; *p < 0.05; **p < 0.01; ***p < 0.001; ****p < 0.0001.

DGKB downregulation contributes to radioresistance by decreasing mitochondrial lipotoxicity

To explore whether DGKB downregulation provided a metabolic advantage for radioresistance, we investigated changes in bioenergetics and biosynthesis. Consistent with our previous studies,[4,5] IR significantly increased the glycolytic rate but reduced the lipid synthesis in U87MG-RR and patient-derived GSCs (Figures S3A and S3B). However, knockdown or overexpression of DGKB did not affect glycolytic rates, RNA synthesis, or lipid synthesis (Figures S3A–S3C). We then assessed β-oxidation by monitoring the release of ^3H_2O from [9,10-^{3}H] oleic acid. Interestingly, by the end of the labeling period (pulse), the release of ^3H_2O was reduced by IR, which was reversed by DGKB overexpression (Figure 4A). After removing oleic acid from the media (chase), the release of ^3H_2O into the media was generally

decreased but DGKB overexpression still increased the release of ^3H_2O, indicating that DGKB facilitates β-oxidation in GBM. Similarly, the $^{14}CO_2$ production from the complete β-oxidation of [1-^{14}C] oleic acid decreased by IR and restored by DGKB overexpression (Figure S3D). Additionally, after IR, the intracellular level of [9,10-^{3}H] oleic acid was unchanged within the first 10 min, which was not affected by DGKB expression, but was increased by 30 min, which was reduced by DGKB expression (Figure 4B). These results indicated that the alteration of β-oxidation after IR was not because of altered cellular uptake of oleic acid and suggested that β-oxidation rather than fatty acid uptake was affected by IR-induced DGKB downregulation. Likewise, as shown in Figure S3E, basal β-oxidation is significantly reduced in U87MG-RR cells compared with parental cells. Collectively, IR-induced DGKB downregulation inhibits β-oxidation in GBM.
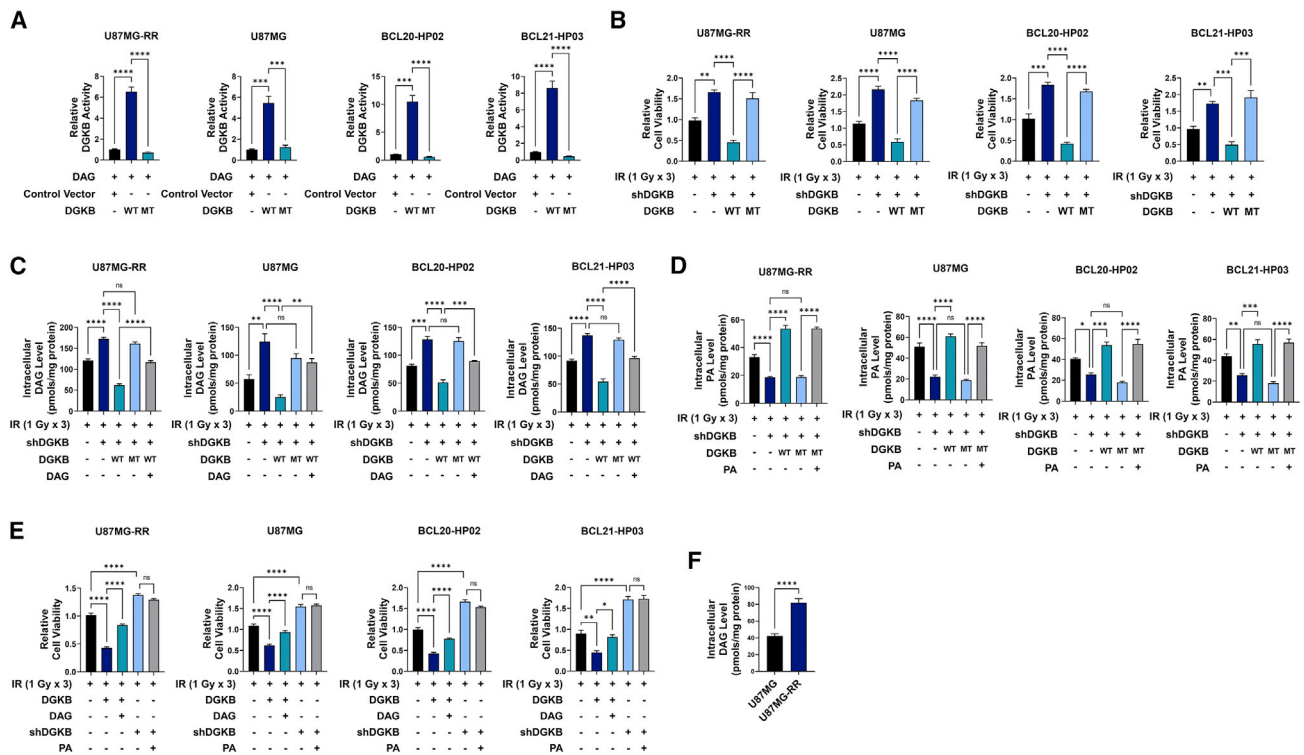
Figure 3. DAG accumulation by downregulation of DGKB contributed to cell viability

(A) The DGKB enzymatic activity in U87MG-RR, U87MG, BCL20-HP02, and BCL21-HP03 without or with ectopic expression of wild-type (WT) or mutant (MT) DGKB.

(B) The cell viability of U87MG-RR, U87MG, BCL20-HP02, and BCL21-HP03 upon IR exposure without or with DGKB knockdown (shDGKB) or with DGKB knockdown together with overexpression of WT or mutant DGKB.

(C and D) Intracellular DAG (C) and PA (D) levels in U87MG-RR, U87MG, BCL20-HP02, and BCL21-HP03 following IR alone or IR together with DGKB modulations as indicated without or with supplementation of DAG (C) or PA (D).

(E) The cell viability of U87MG-RR, U87MG, BCL20-HP02, and BCL21-HP03 following IR alone or together with DGKB overexpression or knockdown without or with supplementation of DAG or PA.

(F) Intracellular DAG levels in U87MG and U87MG-RR. WT, WT DGKB; MT, kinase-dead mutant DGKB (G495D). DGKB knockdown experiments were processed by lentiviral vectors pLKO-Control shRNA or pLKO-shDGKB. All data shown are mean ± SEM of three biological replicates. Statistical analysis was performed with Student's t test for (F) and one-way ANOVA plus a Tukey's multiple comparisons test for the others. ns, non-significant; $*p < 0.05$; $**p < 0.01$; $***p < 0.001$; $****p < 0.0001$.

Because upregulating DGKB activated β-oxidation, we next tested whether upregulating DGKB could increase the ATP level by the activation of β-oxidation. In accordance with the β-oxidation activity, intracellular ATP levels were decreased upon downregulation of DGKB and increased by DGKB overexpression (Figure 4C). However, IR alone significantly increased ATP levels despite the inhibition of β-oxidation induced by DGKB downregulation, probably because other metabolic pathways, such as glucose metabolism, affected cellular bioenergetics. Accordingly, the oxygen consumption rate (OCR) was significantly reduced by DGKB downregulation and increased by its overexpression, whereas the extracellular acidification rate (ECAR) hardly changed (Figures 4D and S3F). Together, downregulation of DGKB attenuated the ATP production generated by β-oxidation.

Recent studies have shown that excessive β-oxidation induces tumor cell death,[23] and that increased storage of TG and LDs can be beneficial for tumor cell survival.[24] Because we confirmed that downregulation of DGKB conferred radiore-

sistance through DAG accumulation, we hypothesized that DAG accumulation might allow acyl-CoA to be used for TG storage rather than β-oxidation to induce radioresistance (Figure 4E). As we expected, TG levels after IR were increased with or without knockdown of DGKB but did not change when DGKB was overexpressed (Figure 4F). Consistent with changes in TG levels, BODIPY staining showed that DGKB knockdown increased LDs, whereas DGKB overexpression diminished LDs after IR (Figure 4G). In correspondence with levels of DAG and TG following DGKB regulation, acyl-CoA (C16:0) and acylcarnitine, which is converted from FAs and shuttled into mitochondria for β-oxidation, were decreased by DGKB knockdown and increased by DGKB overexpression after IR (Figures S3G and S3H). Consequently, the level of acetyl-CoA (C2:0), a major product of FA degradation by β-oxidation, was also decreased by DGKB knockdown and increased by DGKB overexpression after IR (Figure S3I). In sum, radioresistant GBM cells that express low levels of DGKB prefer to store FAs in TG instead of utilizing them as an energy source.
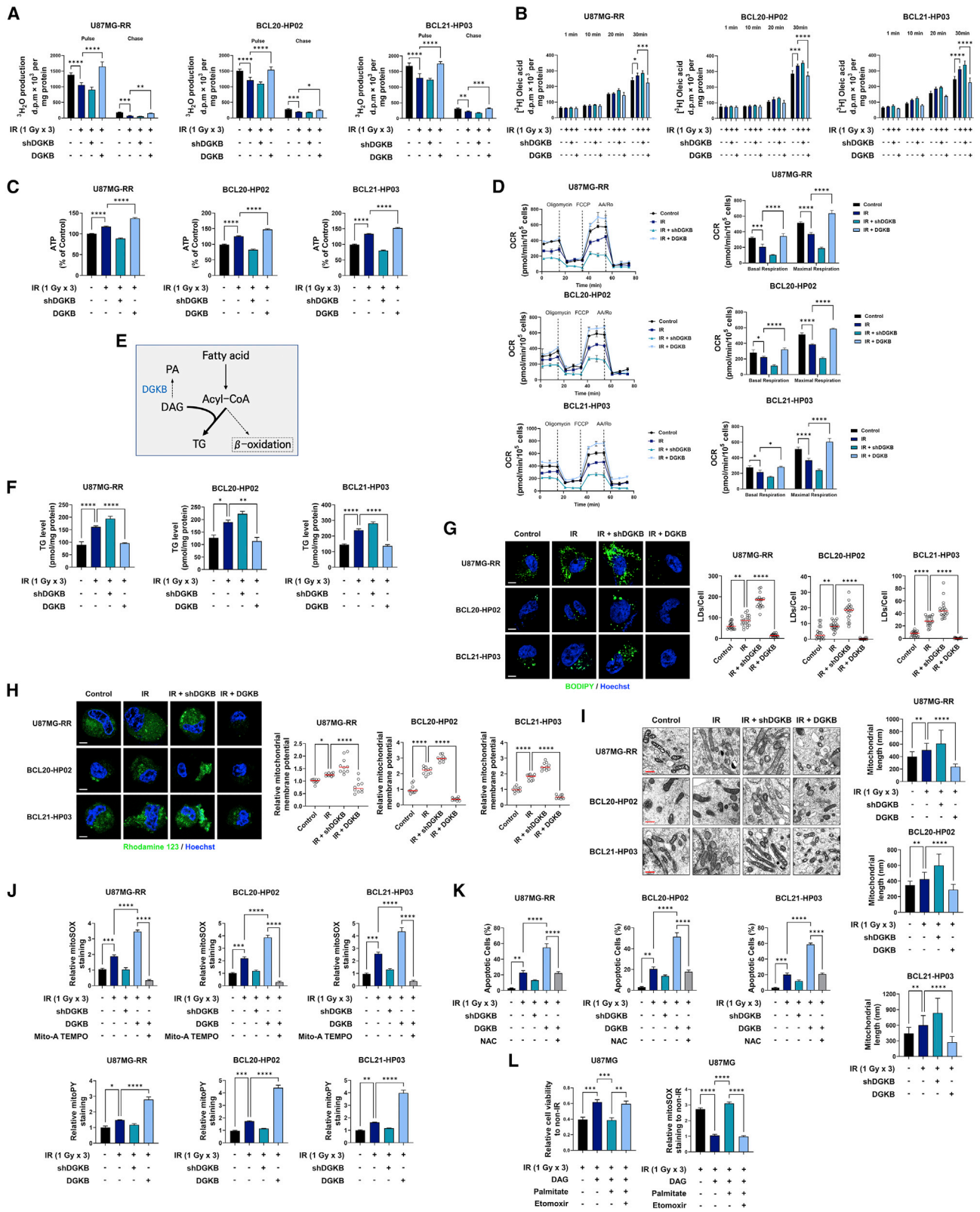
(legend on next page)

Because radioresistant GBM cells prefer not to use FAs as an energy source despite their high energy demand, we hypothesized that excessive β-oxidation might contribute to radiosensitivity. To investigate whether excessive β-oxidation induced mitochondrial dysfunction, we measured mitochondrial membrane potential (MMP). As shown in Figure 4H, DGKB overexpression contributed to aberrant MMP after IR. Likewise, DGKB overexpression severely damaged mitochondria after IR, as determined by transmission electron microscopy (TEM) imaging (Figure 4I). Furthermore, we assessed mitochondrial ROS and H_2O_2 through mitoSOX and mitoPY staining and found that DGKB downregulation attenuated the mitochondrial ROS and H_2O_2 levels, whereas DGKB overexpression highly increased their levels after IR (Figure 4J). However, cellular ROS and H_2O_2 levels were not affected by DGKB overexpression or downregulation after IR (Figures S3J and S3K), suggesting that regulation of DGKB affects ROS and H_2O_2 through β-oxidation in mitochondria. In accordance with ROS and H_2O_2 results, apoptosis was decreased by DGKB downregulation and increased by its overexpression after IR (Figures 4K and S3L). Next, we tested whether DAG accumulation induces radioresistance by reducing β-oxidation-derived ROS. As shown in Figure 4L, treatment of DAG derives radioresistance, but induction of β-oxidation through palmitate treatment diminishes the effect and confers radiosensitivity. Likewise, it was confirmed that mitochondrial ROS is increased by the β-oxidation induction even when DAG is accumulated (Figure 4L). Collectively, DAG accumulation resulting from DGKB downregulation in GBM conferred radioresistance by reducing excessive β-oxidation and inducing the storage of TG and LDs to prevent cell death from mitochondrial ROS.

IR-induced DGAT1 confers radioresistance by increasing TG formation

Because IR-induced DAG accumulation requires the activation of diacylglycerol acyltransferase (DGAT), which catalyzes DAG to TG, to increase the TG formation, we hypothesized that the expression of DGAT was also regulated by IR. We assessed levels of DGAT subtypes (DGAT1 and DGAT2) in U87MG-RR and patient-derived GSCs. Because the lipid metabolism mainly occurs in the liver, we also analyzed the human hepatocellular carcinoma HepG2 cells. DGAT1 expression was overwhelmingly higher than DGAT2 in U87MG-RR and patient-derived GSCs, whereas DGAT1 expression was similar to DGAT2 in HepG2 cells (Figure 5A). Furthermore, higher DGAT1, but not DGAT2, expression in GBM correlated with worse overall survival of GBM patients in the TCGA database (Figure 5B). We therefore then evaluated whether the DGAT1 expression was increased by IR. Consistent with our hypothesis, DGAT1 was increased by IR and its level was higher in U87MG-RR than in the control cells (Figure 5C). Next, we tested whether DGAT1 directly regulates β-oxidation activity. As shown in Figure 5D, DGAT1 knockdown facilitates β-oxidation in GBM, suggesting that IR-induced DGAT1 upregulation inhibits β-oxidation in GBM. In addition, the TG level was significantly reduced by DGAT1 knockdown, with or without DAG addition, in the irradiated GBM cells (Figure 5E). Consequently, knockdown of DGAT1 increased the cell apoptosis after IR, suggesting that inhibition of storing FA induces cell death by excess β-oxidation (Figure 5F).

To investigate the mechanism of IR-induced changes in DGAT1 expression, we performed a luciferase reporter assay to determine the DGAT1 promoter activity and observed no significant change in GBM cells treated with IR (Figure 5G). These results suggested that IR did not increase the transcription of

---

Figure 4. DGKB downregulation contributes to radioresistance by decreasing mitochondrial lipotoxicity

(A) β-Oxidation in U87MG-RR, BCL20-HP02, and BCL21-HP03 assessed by measuring the ^3H_2O production in cells incubated with [9,10-^{3}H] oleic acid during the pulse or chase phase after IR or IR combined with DGKB knockdown or overexpression (24 h). Data are represented as mean ± SEM of three biological replicates.

(B) Evaluation of β-oxidation in U87MG-RR, BCL20-HP02, and BCL21-HP03 by measuring the [9,10-^{3}H] oleic acid remaining in cells incubated with oleic acid after IR or IR combined with DGKB knockdown or overexpression (24 h). Data are represented as mean ± SEM of three biological replicates.

(C) The concentration of ATP in U87MG-RR, BCL20-HP02, and BCL21-HP03 after IR or IR combined with DGKB knockdown or overexpression (24 h). Data are represented as mean ± SEM of three biological replicates.

(D) The OCR of U87MG-RR, BCL20-HP02, and BCL21-HP03 cells cultured in lipidated media after IR or IR combined with DGKB knockdown or overexpression (24 h). Data are represented as mean ± SD of three technical replicates.

(E) A scheme illustrating the pathway of TG synthesis and β-oxidation. DAG, the substrate of DGKB, is metabolized with acyl-CoA to TG synthesis. Acyl-CoA also participates in β-oxidation.

(F) The intracellular TG level in U87MG-RR, BCL20-HP02, and BCL21-HP03 after IR or IR combined with DGKB knockdown or overexpression (72 h). Data are represented as mean ± SEM of three biological replicates.

(G) Representative images and quantification of LDs (n = 30) in U87MG-RR, BCL20-HP02, and BCL21-HP03 through BODIPY staining after IR or IR combined with DGKB knockdown or overexpression (72 h). Scale bars, 5 μm.

(H) Representative images and quantification analysis of MMP (n = 30) in U87MG-RR, BCL20-HP02, and BCL21-HP03 through rhodamine 123 staining after IR or IR combined with DGKB knockdown or overexpression (72 h). Scale bars, 5 μm.

(I) Representative images and mitochondrial length (mean ± SD, n = 30) through TEM imaging in U87MG-RR, BCL20-HP02, and BCL21-HP03 after IR or IR combined with DGKB knockdown or overexpression (72 h). Scale bars, 500 nm.

(J) Mitochondrial ROS and H_2O_2 levels in U87MG-RR, BCL20-HP02, and BCL21-HP03 through mitoSOX (upper graphs) and mitoPY (lower graphs) staining after IR or IR combined with DGKB knockdown or overexpression (72 h) without or with Mito-A TEMPO. Data are represented as mean ± SEM of three biological replicates.

(K) The percentages of apoptotic cell in U87MG-RR, BCL20-HP02, and BCL21-HP03 after IR or IR combined with DGKB knockdown or overexpression (72 h) without or with N-acetyl cysteine (NAC). Data are represented as mean ± SEM of three biological replicates.

(L) The changes in cell viability (left) and mitochondrial ROS (right) after IR, IR with supplementation of DAG, IR with supplementation of DAG and palmitate, or IR with supplementation of DAG, palmitate, and etomoxir in U87MG. Data are represented as mean ± SEM of three biological replicates. Statistical analysis was performed with one-way ANOVA plus a Tukey's multiple comparisons test. *p < 0.05, **p < 0.01, ***p < 0.001, ****p < 0.0001.
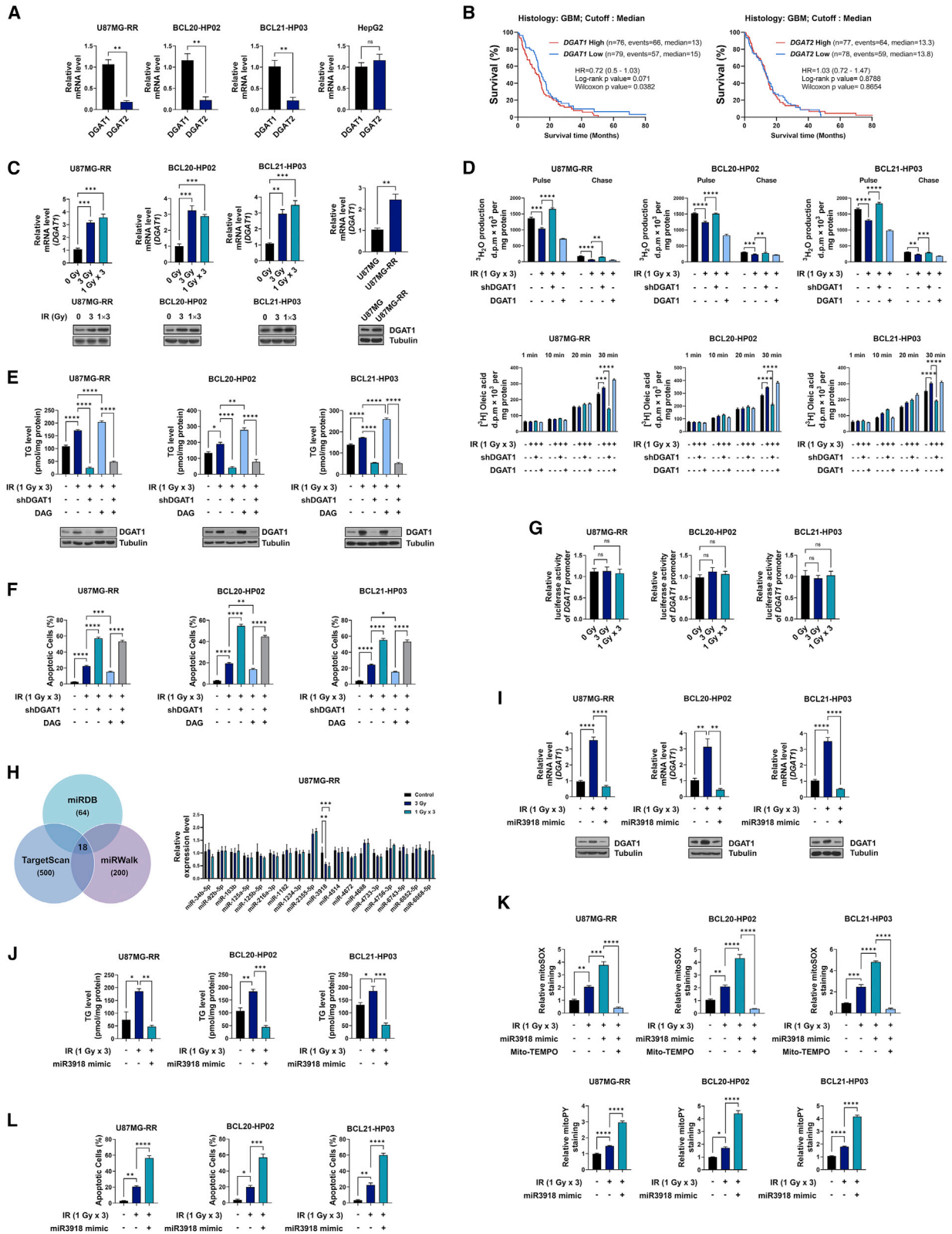
(legend on next page)

DGAT1. Next, we hypothesized that microRNAs (miRNAs) targeting DGAT1 might be changed by IR. We identified 18 miR-NAs as candidates that targeted DGAT1 using miRDB, TargetScan, and miRWalk (Figure 5H, left) but found that only mi-croRNA-3918 (miR-3918) was significantly decreased by IR (Figure 5H, right). To validate that miR-3918 affected the DGAT1 expression, we first confirmed that miR-3918 reduced the expression of a reporter carrying the wild-type 3′ UTR of DGAT1 but not a reporter carrying the 3′UTR of DGAT1 with mutated miR-3918 targeting site (Figures S4A and S4B). We then found that miR-3918 effectively inhibited IR-induced DGAT1 expression in GBM (Figure 5I). Consistent with the effect of the knockdown data, miR-3918 suppressed TG levels (Figure 5J) and induced ROS and H_2O_2 production (Figure 5K) and apoptosis after IR (Figure 5L). Likewise, acylcarnitine and acetyl-CoA levels were rescued by miR-3918 after IR (Figures S5A and S5B). These results together showed that DGAT1 attenuated β-oxidation through TG formation and that miR-3918, which targets DGAT1, contributed to sensitizing the IR effect through DGAT1 inhibition.

Genetic inhibition of DGAT1 significantly suppresses radioresistance and prolongs overall survival in GBM xenograft mouse models

To examine the role of DGAT1 in vivo, we established orthotopic xenograft GBM mouse models using U87MG-RR and BCL21-HP03 cells, then treated tumor-bearing mice with IR together with shDGAT1 or lentiviral-miR-3918 mimic (Figure 6A). In vivo bioluminescent imaging showed that, compared with IR alone, IR combined with shDGAT1 or miR-3918 reduced U87MG-RR tumor growth by 65.34% or 53.64%, respectively, and reduced BCL21-HP03 tumor growth by 64.48% or 52.94%, respectively (Figures 6B and 6C). Consistently, H&E staining showed that tumor size was remarkably decreased by IR combined with DGAT1 knockdown or miR-3918 treatment (Figure 6D). Moreover, the DGAT1 level was highly increased by IR and DGAT1 knockdown or miR-3918 treatment markedly enhanced IR-induced apoptosis, as determined by IHC staining of cleaved caspase 3 (Figure 6E). Consistent with our in vitro analysis, LDs were increased by IR, which was decreased by DGAT1 knockdown or miR-3918 treatment, as determined by immunofluorescence (IF) staining of TIP47, suggesting that lipotoxicity induced by β-oxidation increased under conditions of DGAT1 downregulation. Consequently, the overall survival of mice with U87MG-RR xenografts was significantly improved by IR combined with DGAT1 downregulation compared with untreated control (28 days of median survival) or IR alone (30 days of median survival) (Figure 6F). Likewise, the overall survival of mice with BCL21-HP03 xenografts was significantly improved by IR combined with DGAT1 downregulation compared with untreated control (19 days of median survival) or IR alone (25 days of median survival). Notably, because a previous study showed that DGAT1 knockdown solely suppressed tumor growth, we established orthotopic xenograft GBM mouse models using U87MG-RR untreated control cells and shDGAT1-treated cells then treated tumor-bearing mice with IR. Although DGAT1 knockdown alone reduced the tumor growth to some extent, shDGAT1 combined with IR reduced the tumor growth by 48.82% compared with shDGAT1 alone (Figures S6A and S6B). Consequently, the overall survival of mice with U87MG-RR xenografts was significantly improved by shDGAT1 combined with IR compared with untreated control (27 days of median survival) or shDGAT1 alone (33 days of median survival) (Figure S6C). Collectively, DGAT1 downregulation by its short hairpin RNA (shRNA) or miR-3918 significantly reduced radioresistance and extended overall survival in both models.

Figure 5. IR-induced DGAT1 confers radioresistance by increasing TG formation

(A) Relative mRNA levels of DGAT1 and DGAT2 in U87MG-RR, BCL20-HP02, BCL21-HP03, and HepG2. Data are represented as mean ± SEM of three biological replicates.

(B) Kaplan-Meier survival plots of individuals with GBM in TCGA database based on DGAT1 and DGAT2 mRNA levels.

(C) The mRNA and protein levels of DGAT1 in U87MG-RR, BCL20-HP02, and BCL21-HP03 with IR (single 3 Gy or 1 Gy in three fractions) (left three graphs) and in U87MG versus U87MG-RR (the right graph). Data are represented as mean ± SEM of three biological replicates.

(D) β-Oxidation in U87MG-RR, BCL20-HP02, and BCL21-HP03 assessed by measuring the ^3H_2O production in cells incubated with [9,10-^{3}H] oleic acid during the pulse or chase phase after IR or IR combined with DGAT1 knockdown or overexpression (24 h, upper graphs) and evaluation of β-oxidation in U87MG-RR, BCL20-HP02, and BCL21-HP03 by measuring the [9,10-^{3}H] oleic acid remaining in cells incubated with oleic acid after IR or IR combined with DGAT1 knockdown or overexpression (24 h, lower graphs). Data are represented as mean ± SEM of three biological replicates.

(E) The TG level (upper graphs) and the DGAT1 protein level (lower) in U87MG-RR, BCL20-HP02, and BCL21-HP03 after IR, or IR combined with DGAT1 knockdown without or with DAG supplementation. Data are represented as mean ± SEM of three biological replicates.

(F) The percentages of apoptotic U87MG-RR, BCL20-HP02, and BCL21-HP03 cells after IR, or IR combined with DGAT1 knockdown without or with DAG supplementation. Data are represented as mean ± SEM of three biological replicates.

(G) The relative luciferase activity in U87MG-RR, BCL20-HP02, and BCL21-HP03 expressing a DGAT1 promoter reporter after IR (single 3 Gy or 1 Gy in three fractions). Data are represented as mean ± SEM of three biological replicates.

(H) Venn diagram of DGAT1-targeting miRNAs predicted from miRDB, TargetScan, and miRWalk and a bar graph showing relative levels of the 18 overlapped miRNAs in U87MG-RR after IR (single 3 Gy or 1 Gy in three fractions). Data are represented as mean ± SEM of three biological replicates.

(I) The mRNA and protein levels of DGAT1 in U87MG-RR, BCL20-HP02, and BCL21-HP03 after IR or IR combined with miR-3918 mimic. Data are represented as mean ± SEM of three biological replicates.

(J) The TG level in U87MG-RR, BCL20-HP02, and BCL21-HP03 after IR or IR combined with miR-3918 mimic. Data are represented as mean ± SEM of three biological replicates.

(K) Mitochondrial ROS and H_2O_2 levels in U87MG-RR, BCL20-HP02, and BCL21-HP03 through mitoSOX (upper) and mitoPY (lower) staining after IR or IR combined with miR-3918 mimic. Data are represented as mean ± SEM of three biological replicates.

(L) The percentage of apoptotic U87MG-RR, BCL20-HP02, and BCL21-HP03 cell after IR or IR combined with miR-3918 mimic. Data are represented as mean ± SEM of three biological replicates. Statistical analysis was performed with Student's t test for (A) and (C, right graph), Log rank (Mantel-Cox) test for (B) and one-way ANOVA plus a Tukey's multiple comparisons test for the others. ns, non-significant; *$p < 0.05$; **$p < 0.01$; ***$p < 0.001$; ****$p < 0.0001$.
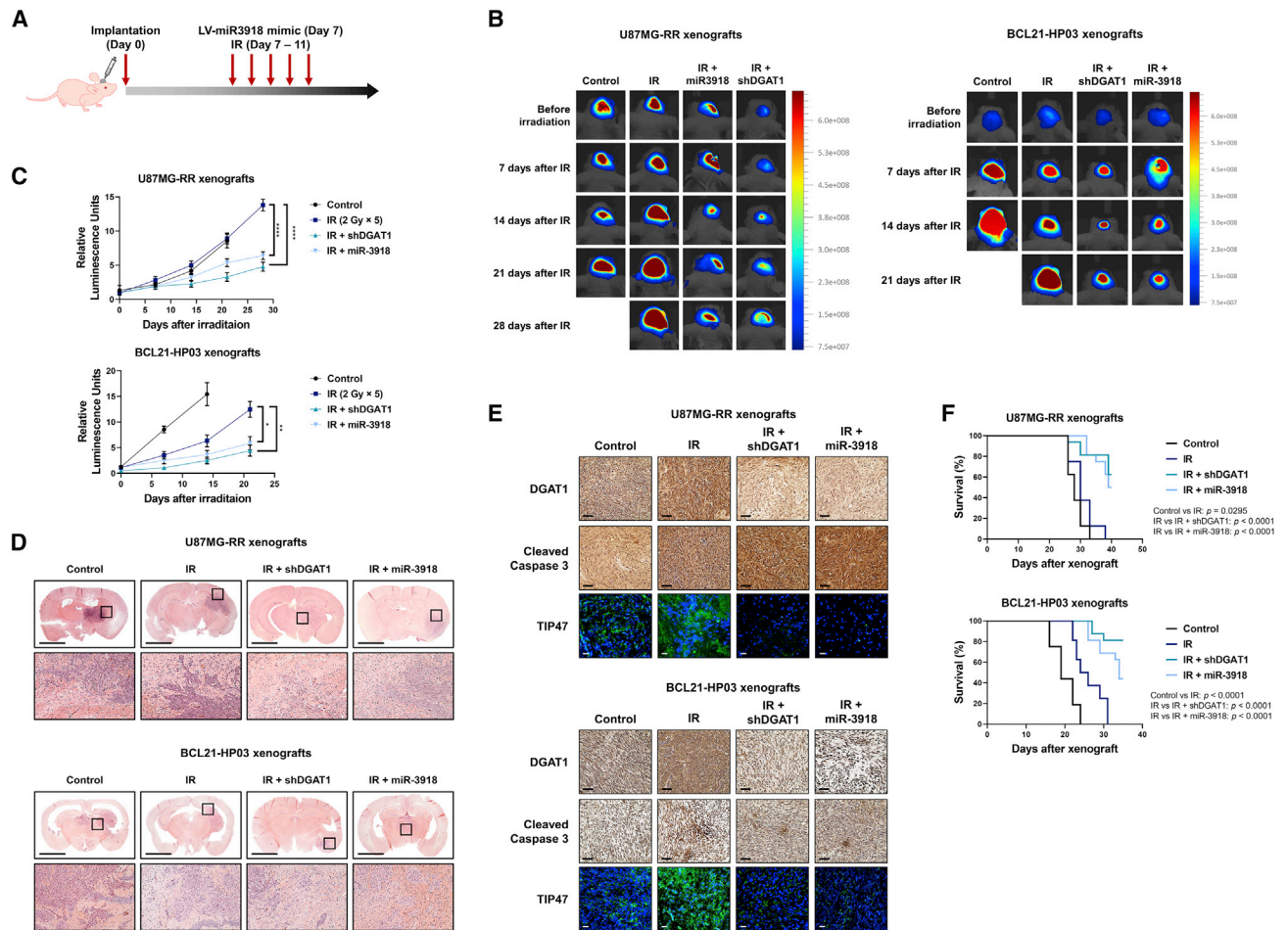
Figure 6. Genetic inhibition of DGAT1 significantly suppresses radioresistance and prolongs overall survival in GBM xenograft mouse models

(A) The schedule of U87MG-RR or BCL21-HP03 orthotopic xenograft mouse model treated with IR together with shDGAT1 or miR-3918.

(B) *In vivo* bioluminescent images of orthotopic xenografts derived from U87MG-RR and BCL21-HP03 in control mice and in mice treated with IR or IR together with miR-3918 or shRNA (n = 16).

(C) The relative luminescence units of orthotopic xenograft derived from U87MG-RR and BCL21-HP03 in control mice, with IR or IR together with miR-3918 or shRNA.

(D) Representative H&E staining images of orthotopic U87MG-RR and BCL21-HP03 xenograft tissues with control, IR, IR combined with DGAT1 knockdown, and IR together with miR-3918. Scale bars, 2,000 μm.

(E) Representative images of IHC for DGAT1 or cleaved caspase 3 and IF for TIP47 in tumor tissues from mice orthotopically xenografted with U87MG-RR and BCL21-HP03 then without (control) or with IR, IR combined with DGAT1 knockdown, or IR combined with miR-3918. Scale bars, 50 μm (upper) or 20 μm (lower).

(F) Kaplan-Meier survival curve of mice with orthotopic U87MG-RR or BCL21-HP03 xenograft untreated (control) or treated with IR, IR combined with DGAT1 knockdown, and IR together with miR-3918 (IR treatments started 7 days after xenograft). Statistical analysis was performed with one-way ANOVA plus a Tukey's multiple comparisons test for (C) compared with luminescence values of IR alone at 28 days after irradiation, and Log rank (Mantel-Cox) test for (F). ns, non-significant; *$p < 0.05$; **$p < 0.01$; ****$p < 0.0001$.

Pharmacological alteration of DGKB and DGAT1 expressions sensitizes GBM cells to IR and attenuates tumor growth in GBM xenograft mouse models

Although TMZ is the only chemotherapeutic agent currently used in GBM patients, approximately half of treated patients do not respond to TMZ due to their tumors overexpressing O^6-methylguanine-DNA methyltransferase (MGMT).[25] Moreover, most drugs developed for GBM treatment over the past 20 years failed in clinical trials due to various challenges, including inefficient drug delivery and severe side effects. In

this regard, we investigated existing blood-brain barrier (BBB)-penetrating radiosensitizers with dual functions of activating DGKB and inhibiting DGAT1 by interrogating The Connectivity Map (CMap).[26] Of the various candidates, we found that cladribine (2-chloro-2′-deoxyadenosine), a US Food and Drug Administration (FDA)-approved drug for leukemia, showed the best enrichment scores and significantly increased the DGKB mRNA level and decreased the DGAT1 mRNA level (Figure 7A). We then tested whether mRNA levels of DGKB and DGAT1 were regulated by cladribine treatment in U87MG-RR
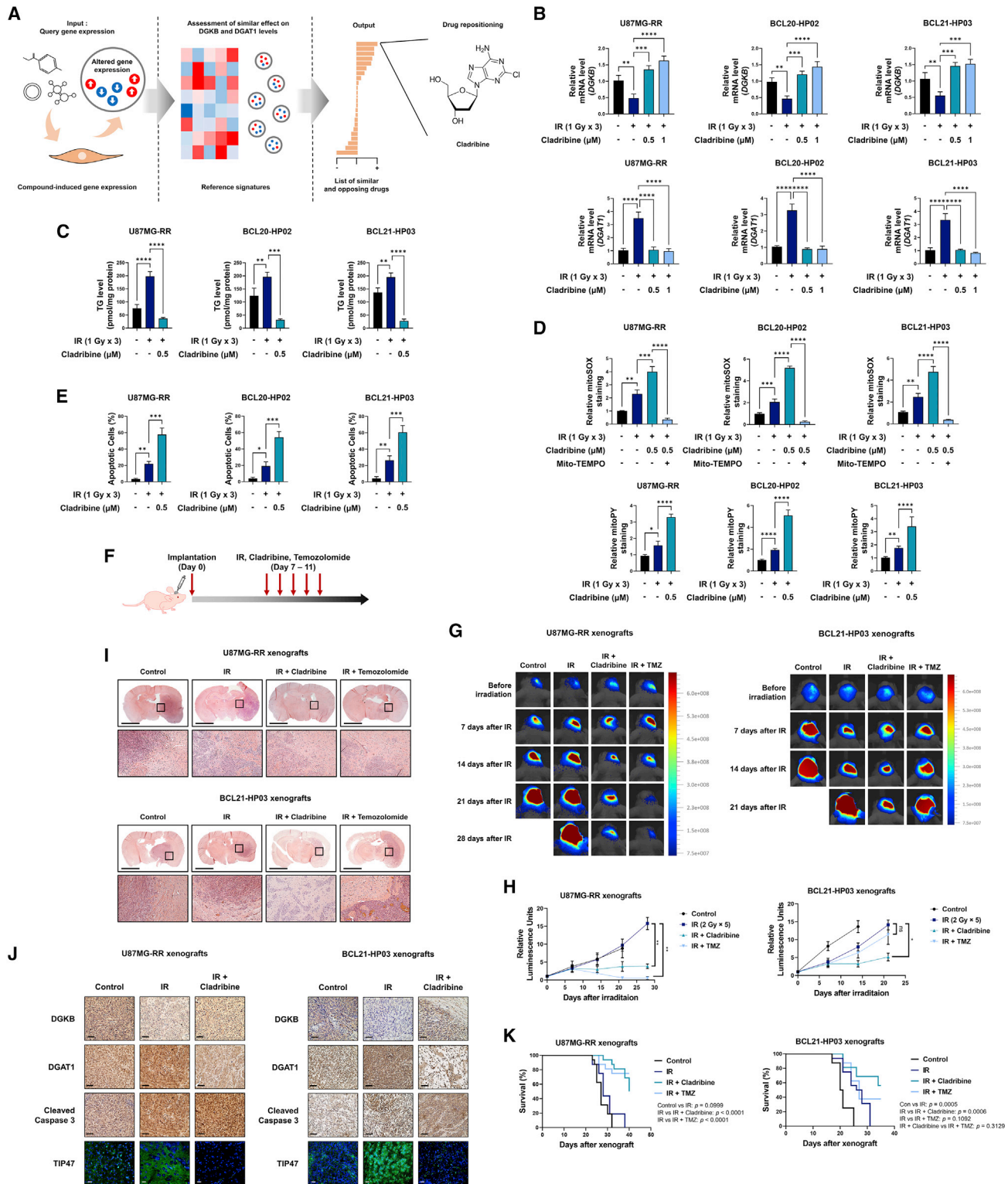
(legend on next page)

cells and patient-derived GSCs. Cladribine significantly increased DGKB and decreased DGAT1 mRNA levels (Figure 7B) and increased the TG level after IR (Figure 7C). Moreover, cladribine treatment increased mitochondrial ROS and H_2O_2 levels (Figure 7D) and apoptosis (Figure 7E) after IR. To determine whether cladribine can affect tumor growth *in vivo* and animal survival, we established orthotopic xenograft GBM mouse models using U87MG-RR and BCL21-HP03 cells and treated them with IR or IR combined with cladribine or TMZ (Figure 7F). *In vivo* bioluminescent imaging showed that cladribine markedly sensitized the GBM cells to IR in both models (Figures 7G and 7H). When combined with IR, TMZ was more effective than cladribine in inhibiting the growth of U87MG-RR-driven tumors (reduced by 96.67% and 75.78%, respectively) but was less effective than cladribine in BCL21-HP03-driven tumors (reduced by 18.97% and 63.43%, respectively). This difference presumably is because that U87MG-RR cells are MGMT negative, whereas BCL21-HP03 cells are MGMT positive. Likewise, H&E staining showed that tumor size was remarkably decreased by IR combined with cladribine (Figure 7I). Moreover, consistent with our *in vitro* analysis, cladribine restored IR-induced DGKB downregulation and reduced IR-induced DGAT1 (Figure 7J). Likewise, cladribine increased the level of cleaved caspase 3 and decreased TIP47 after IR, indicating that cladribine highly sensitizes GBM cells to IR by reducing LDs and promoting apoptosis. Consequently, overall survival of tumor-bearing mice was significantly improved by IR combined with cladribine compared with untreated control (20.5 days of median survival) or IR alone (27 days of median survival), and it was much more effective than TMZ combined with IR (27 days of median survival) in BCL21-HP03 xenografts (Figure 7K). Collectively, cladribine induced DGKB upregulation and DGAT1 downregulation, significantly sensitized GBM cells to IR, decreased tumor growth, and increased overall survival in both models.

DISCUSSION

Rewiring of lipid metabolism is important for ATP production and maintenance of redox homeostasis in GBM. However, how GBM cells acquire radioresistance by regulating lipid metabolism has not been elucidated. In this study, we demonstrate that radioresistant GBM cells maintain lipid homeostasis through DGKB downregulation and DGAT1 upregulation to reduce the FA oxidation-mediated ROS after radiation. DGKB knockdown or the expression of DGKB kinase-dead mutant induces DAG accumulation and IR-induced DGAT1 promotes the accumulation of TGs and LDs to prevent FAs from entering the mitochondria to undergo FA oxidation. Conversely, DGKB overexpression or DGAT1 inhibition by miR-3918 mimic activates FA oxidation to increase ROS-induced mitochondrial damage and GBM cell radiosensitivity. Additionally, cladribine, which increases the expression of DGKB and decreases that of DGAT1, significantly improves the survival of GBM-bearing mice in combination with IR, indicating that targeting the lipid homeostasis could be a promising strategy to overcome radioresistance of GBM.

Reprogramming of the lipid metabolism is closely linked to alterations in energy production by FA oxidation. Because the mitochondrial electron transport chain is a major source of ROS production and GBM tissue contains large amounts of TGs,[13] FA oxidation can be harmful due to the unavoidable production of ROS in GBM cells. In this regard, therapeutic approaches promoting lipid catabolism can possibly be effective when the ROS levels cross the death threshold.[27,28] Notably, antioxidant-related genes are highly upregulated in our radioresistant GBM cell model according to the RNA-sequencing analysis. For example, the level of manganese superoxide dismutase (MnSOD) increases by 3.778-fold and the interleukin (IL) 6 level increases by 12.394-fold in U87MG-RR cells compared with their parental cells. MnSOD is the main antioxidant enzyme protecting cells from mitochondrial ROS, and a recent study shows that the

---

Figure 7. Pharmacological regulation of DGKB and DGAT1 sensitizes GBM cells to IR and attenuates tumor growth in GBM xenograft mouse models

(A) A scheme illustrating the screening to identify cladribine through The Connectivity Map (CMap, BROAD Institute).

(B) The relative mRNA level of DGKB (left) and DGAT1 (right) in U87MG-RR, BCL20-HP02, and BCL21-HP03 after IR or IR combined with cladribine. Data are represented as mean ± SEM of three biological replicates.

(C) The level of TG in U87MG-RR, BCL20-HP02, and BCL21-HP03 after IR or IR combined with cladribine. Data are represented as mean ± SEM of three biological replicates.

(D) Mitochondrial ROS and H_2O_2 levels in U87MG-RR, BCL20-HP02, and BCL21-HP03 through mitoSOX (upper) and mitoPY (lower) staining after IR or IR combined with cladribine. Data are represented as mean ± SEM of three biological replicates.

(E) The percentages of apoptotic U87MG-RR, BCL20-HP02, and BCL21-HP03 cells after IR or IR combined with cladribine. Data are represented as mean ± SEM of three biological replicates.

(F) The schedule of U87MG-RR or BCL21-HP03 orthotopic xenograft mouse model treated with IR or IR together with cladribine or TMZ.

(G) *In vivo* bioluminescent images of orthotopic xenografts derived from U87MG-RR and BCL21-HP03 in control mice or mice treated with IR or IR together with cladribine or TMZ (n = 16).

(H) The relative luminescence units of orthotopic xenograft derived from U87MG-RR and BCL21-HP03 in control mice or mice treated with IR or IR together with cladribine or TMZ.

(I) Representative H&E staining images of orthotopic U87MG-RR and BCL21-HP03 xenograft tissues from control mice or mice treated IR or IR together with cladribine or TMZ. Scale bars, 2,000 μm.

(J) Representative images of IHC staining for DGKB, DGAT1, and cleaved caspase 3 and IF images of TIP47 in orthotopic U87MG-RR and BCL21-HP03 xenograft tissues from control mice or mice treated with IR or IR together with cladribine or TMZ. Scale bars, 50 μm (upper) or 20 μm (lower).

(K) Kaplan-Meier survival curve of mice with orthotopic U87MG-RR and BCL21-HP03 xenograft without treatment (control) or treated with IR or IR together with cladribine or TMZ (IR treatments started 7 days after xenograft). Statistical analysis was performed with one-way ANOVA plus a Tukey's multiple comparisons test for (B)–(E). In addition, one-way ANOVA plus a Tukey's multiple comparisons test for (H) compared with luminescence values of IR alone at 28 days after irradiation, and Log rank (Mantel-Cox) test for (K). ns, non-significant; *p < 0.05; **p < 0.01; ***p < 0.001; ****p < 0.0001.

increased activity of MnSOD improves cell viability after IR and induces radioresistance.[29] Furthermore, treating glioma cells with IL6 has been shown to induce radioresistance by reducing mitochondrial ROS.[30] Thus, our RNA-sequencing data support the fact that radioresistant GBM cells prefer to store FAs rather than use them for energy production to minimize damage from mitochondrial ROS.

Cladribine is a synthetic purine nucleoside analogue that is approved by the FDA to treat hairy cell leukemia and B cell chronic lymphocytic leukemia as well as multiple sclerosis, supporting that cladribine is safe for CNS functioning. Cladribine is phosphorylated by deoxycytidine kinase (DCK) to cladribine triphosphate instead of being broken down by adenosine deaminase. Cladribine triphosphate is then incorporated into and accumulates in DNA, resulting in an imbalanced triphosphorylated deoxynucleotide (dNTP) pools and subsequent apoptosis. Therefore, the more a cell accumulates intracellular cladribine triphosphate, the more vulnerable it is to cladribine-mediated apoptosis. The accumulation of cladribine triphosphate depends on the ratio of DCK to 5′-nucleotidase, which turns cladribine triphosphate back to the inactive cladribine. The DCK to 5′-nucleotidase ratio is high in immune cells but is considerably low in other cell types, including glial cells.[31] Cladribine triphosphate is therefore hardly accumulated in GBM cells. Indeed, our cell viability data show that the half maximal inhibitory concentration (IC_{50}) of cladribine is significantly higher in U87MG-RR than that in THP-1 cells (Figure S7A). However, our results show that cladribine triggers ROS-induced apoptosis by regulating the expression of DGKB and DGAT1, indicating that unphosphorylated cladribine may have a role in GBM cells independent of its conventional function. In addition, as an FDA-approved oral drug, side effects of cladribine are quite manageable and it has been well evaluated for pharmacokinetics and efficacy in previous clinical trials.[31,32] According to Cladribine Tablets Treating Multiple Sclerosis Orally (CLARITY) and CLARITY Extension, approximately 90% of actively treated patients completed each study, and there were relatively few study discontinuations due to adverse effects.[33] Moreover, the bioavailability of oral cladribine is 37%–51% compared with subcutaneous administration and the terminal half-life of cladribine is 5.7–19.7 h.[34] Furthermore, cladribine effectively penetrates the BBB, and approximately 25% of the plasma concentration of cladribine reaches the cerebrospinal fluid (CSF).[34] The effects of cladribine are sustained for more than 10 months following the last dose of both parenteral cladribine and oral cladribine tablets.[31] Therefore, the pharmacokinetics of cladribine may not limit its application to GBM therapy.

Overall, our study suggests that radioresistant GBM cells efficiently prevent mitochondrial lipotoxicity by downregulating DGKB and upregulating DGAT1, and provides a strong basis to regulate them for clinical application against GBM. DGKB has also been reported to play a major role in the small intestine,[35] and our results show that the expression of DGAT1 is also upregulated by IR in other cancers such as pancreas, lung, and gallbladder, so it will be important to determine whether targeting either or both enzymes affects other cancer types (Figure S4C). Considering our preclinical data from xenograft mouse models using the established radioresistant GBM cells and MGMT-positive GSCs, regulating DGKB and DGAT1 or repurposing cladribine for GBM treatment may overcome resistance to conventional therapies.

Limitations of the study

Despite the considerable radiosensitizing effect of cladribine, the mechanism of its regulatory effect on DGKB and DGAT1 is still unclear. Thus, further studies are needed to identify the mechanism that can translate our findings to the clinic for the treatment of GBM. Nevertheless, most drugs developed for GBM treatment failed over the past 20 years in clinical trials due to inefficient drug delivery and severe side effects even though the mechanisms have been elucidated. Our goal was to discover a radiosensitizing drug that has manageable side effects and the ability to penetrate the BBB. We believe that its clinical trials to treat GBM may demonstrate a long-term benefit and therapeutic value for GBM patients.

Another limitation of this study is that we only used GBM xenograft mouse models but not syngeneic GBM mouse models. Even though xenograft mouse models are more generally used in GBM studies than syngeneic mouse models,[36] the effect of the immune system on radioresistance can be neglected when immunodeficient mice are used. Notably, because cladribine preferentially targets B and T lymphocytes, there is a need to investigate the radiosensitizing effect of cladribine using immunocompetent syngeneic GBM mouse models. Touching on this issue, it will be possible not only to verify the efficacy of cladribine as a radiosensitizer but also to elucidate the relationship between radioresistance and the immune system in GBM.

STAR★METHODS

Detailed methods are provided in the online version of this paper and include the following:

- KEY RESOURCES TABLE
- RESOURCE AVAILABILITY
  - Lead contact
  - Materials availability
  - Data and code availability
- EXPERIMENTAL MODEL AND SUBJECT DETAILS
  - Glioblastoma stem cell derivation
  - Establishment of radioresistant cells
  - Animal care protocol and orthotopic xenograft mouse model
  - Cell lines, cell culture, and irradiation
- METHOD DETAILS
  - RNA-sequencing
  - Analysis of GBM poor prognosis-related genes
  - Quantitative real-time PCR
  - Western blots
  - Lentiviral transduction
  - Cell viability assay and colony-forming assay
  - Mouse bioluminescence imaging
  - Hematoxylin and Eosin (H&E) and Immunohistochemistry (IHC) staining
  - Enzyme activity assay
  - LC-MS/MS lipid profiling

- ○ Metabolic assays
- ○ Fatty acid oxidation
- ○ Seahorse analysis
- ○ Lipid droplet staining and quantification
- ○ Mitochondrial membrane potential
- ○ Transmission Electronic microscopy (TEM)
- ○ Reactive oxygen species detection
- ○ Mitochondria and cytosol fractionation
- ○ Apoptosis assay (Annexin V/PI)
- ○ Luciferase reporter gene assay
- ○ Intracerebral injection procedures
- ● QUANTIFICATION AND STATISTICAL ANALYSIS

SUPPLEMENTAL INFORMATION

ACKNOWLEDGMENTS

AUTHOR CONTRIBUTIONS

Conceptualization, H.Y. and B.Y.; software, H.L.; validation, E.S., Byeongsoo Kim, and J.K.; formal analysis, H.K. and H.L.; investigation, H.K., H.L., K.K., and H.Y.; resources, Bohkyung Kim, J.S.L., J.L., and H.Y.; writing – original draft, H.K. and H.L.; writing – review & editing, B.Y.; supervision, B.Y.; funding acquisition, B.Y.

DECLARATION OF INTERESTS

The authors declare no competing interests.

REFERENCES

1. Weller, M., Cloughesy, T., Perry, J.R., and Wick, W. (2013). Standards of care for treatment of recurrent glioblastoma–are we there yet? Neuro Oncol. *15*, 4–27. https://doi.org/10.1093/neuonc/nos273.

2. Rapp, M., Baernreuther, J., Turowski, B., Steiger, H.J., Sabel, M., and Kamp, M.A. (2017). Recurrence pattern analysis of primary glioblastoma. World Neurosurg. *103*, 733–740. https://doi.org/10.1016/j.wneu.2017.04.053.

3. Sobanski, T., Rose, M., Suraweera, A., O'Byrne, K., Richard, D.J., and Bolderson, E. (2021). Cell metabolism and DNA repair pathways: implications for cancer therapy. Front. Cell Dev. Biol. *9*, 633305. https://doi.org/10.3389/fcell.2021.633305.

4. Son, B., Lee, S., Kim, H., Kang, H., Jeon, J., Jo, S., Seong, K.M., Lee, S.J., Youn, H., and Youn, B. (2020). Decreased FBP1 expression rewires metabolic processes affecting aggressiveness of glioblastoma. Oncogene *39*, 36–49. https://doi.org/10.1038/s41388-019-0974-4.

5. Kang, H., Lee, S., Kim, K., Jeon, J., Kang, S.G., Youn, H., Kim, H.Y., and Youn, B. (2021). Downregulated CLIP3 induces radioresistance by enhancing stemness and glycolytic flux in glioblastoma. J. Exp. Clin. Cancer Res. *40*, 282. https://doi.org/10.1186/s13046-021-02077-4.

6. Tang, L., Wei, F., Wu, Y., He, Y., Shi, L., Xiong, F., Gong, Z., Guo, C., Li, X., Deng, H., et al. (2018). Role of metabolism in cancer cell radioresistance and radiosensitization methods. J. Exp. Clin. Cancer Res. *37*, 87. https://doi.org/10.1186/s13046-018-0758-7.

7. Lin, H., Patel, S., Affleck, V.S., Wilson, I., Turnbull, D.M., Joshi, A.R., Maxwell, R., and Stoll, E.A. (2017). Fatty acid oxidation is required for the respiration and proliferation of malignant glioma cells. Neuro Oncol. *19*, 43–54. https://doi.org/10.1093/neuonc/now128.

8. Geng, F., Cheng, X., Wu, X., Yoo, J.Y., Cheng, C., Guo, J.Y., Mo, X., Ru, P., Hurwitz, B., Kim, S.H., et al. (2016). Inhibition of SOAT1 suppresses glioblastoma growth via blocking SREBP-1-mediated lipogenesis. Clin. Cancer Res. *22*, 5337–5348. https://doi.org/10.1158/1078-0432.Ccr-15-2973.

9. Guo, D., and Guo, D. (2017). Lipid droplets, potential biomarker and metabolic target in glioblastoma. Intern. Med. Rev. *3*. https://doi.org/10.18103/imr.v3i5.443.

10. Duman, C., Yaqubi, K., Hoffmann, A., Acikgöz, A.A., Korshunov, A., Bendszus, M., Herold-Mende, C., Liu, H.K., and Alfonso, J. (2019). Acyl-CoA-binding protein drives glioblastoma tumorigenesis by sustaining fatty acid oxidation. Cell Metab. *30*, 274–289.e5. https://doi.org/10.1016/j.cmet.2019.04.004.

11. Wu, X., Geng, F., Cheng, X., Guo, Q., Zhong, Y., Cloughesy, T.F., Yong, W.H., Chakravarti, A., and Guo, D. (2020). Lipid droplets maintain energy homeostasis and glioblastoma growth via autophagic release of stored fatty acids. iScience *23*, 101569. https://doi.org/10.1016/j.isci.2020.101569.

12. Koundouros, N., and Poulogiannis, G. (2020). Reprogramming of fatty acid metabolism in cancer. Br. J. Cancer *122*, 4–22. https://doi.org/10.1038/s41416-019-0650-z.

13. Cheng, X., Geng, F., Pan, M., Wu, X., Zhong, Y., Wang, C., Tian, Z., Cheng, C., Zhang, R., Puduvalli, V., et al. (2020). Targeting DGAT1 ameliorates glioblastoma by increasing fat catabolism and oxidative stress. Cell Metab. *32*, 229–242.e8. https://doi.org/10.1016/j.cmet.2020.06.002.

14. Cheng, X., Geng, F., and Guo, D. (2020). DGAT1 protects tumor from lipotoxicity, emerging as a promising metabolic target for cancer therapy. Mol. Cell. Oncol. *7*, 1805257. https://doi.org/10.1080/23723556.2020.1805257.

15. Nogueira, V., and Hay, N. (2013). Molecular pathways: reactive oxygen species homeostasis in cancer cells and implications for cancer therapy. Clin. Cancer Res. *19*, 4309–4314. https://doi.org/10.1158/1078-0432.Ccr-12-1424.

16. Mérida, I., Torres-Ayuso, P., Ávila-Flores, A., Arranz-Nicolás, J., Andrada, E., Tello-Lafoz, M., Liébana, R., and Arcos, R. (2017). Diacylglycerol kinases in cancer. Adv. Biol. Regul. *63*, 22–31. https://doi.org/10.1016/j.jbior.2016.09.005.

17. Tu-Sekine, B., and Raben, D.M. (2011). Regulation and roles of neuronal diacylglycerol kinases: a lipid perspective. Crit. Rev. Biochem. Mol. Biol. *46*, 353–364. https://doi.org/10.3109/10409238.2011.577761.

18. Shirai, Y., and Saito, N. (2014). Diacylglycerol kinase as a possible therapeutic target for neuronal diseases. J. Biomed. Sci. *21*, 28. https://doi.org/10.1186/1423-0127-21-28.

19. Massart, J., and Zierath, J.R. (2019). Role of diacylglycerol kinases in glucose and energy homeostasis. Trends Endocrinol. Metab. *30*, 603–617. https://doi.org/10.1016/j.tem.2019.06.003.

20. Caricasole, A., Bettini, E., Sala, C., Roncarati, R., Kobayashi, N., Caldara, F., Goto, K., and Terstappen, G.C. (2002). Molecular cloning and

characterization of the human diacylglycerol kinase beta (DGKbeta) gene: alternative splicing generates DGKbeta isotypes with different properties. J. Biol. Chem. *277*, 4790–4796. https://doi.org/10.1074/jbc.M110249200.

21. Shirai, Y., Kouzuki, T., Kakefuda, K., Moriguchi, S., Oyagi, A., Horie, K., Morita, S.Y., Shimazawa, M., Fukunaga, K., Takeda, J., et al. (2010). Essential role of neuron-enriched diacylglycerol kinase (DGK), DGKbeta in neurite spine formation, contributing to cognitive function. PLoS One *5*, e11602. https://doi.org/10.1371/journal.pone.0011602.

22. Tsushima, S., Kai, M., Yamada, K., Imai, S.i., Houkin, K., Kanoh, H., and Sakane, F. (2004). Diacylglycerol kinase gamma serves as an upstream suppressor of Rac1 and lamellipodium formation. J. Biol. Chem. *279*, 28603–28613. https://doi.org/10.1074/jbc.M314031200.

23. Tang, D.G., La, E., Kern, J., and Kehrer, J.P. (2002). Fatty acid oxidation and signaling in apoptosis. Biol. Chem. *383*, 425–442. https://doi.org/10.1515/bc.2002.046.

24. Cruz, A.L.S., Barreto, E.d.A., Fazolini, N.P.B., Viola, J.P.B., and Bozza, P.T. (2020). Lipid droplets: platforms with multiple functions in cancer hallmarks. Cell Death Dis. *11*, 105. https://doi.org/10.1038/s41419-020-2297-3.

25. Kang, H., Lee, H., Kim, D., Kim, B., Kang, J., Kim, H.Y., Youn, H., and Youn, B. (2022). Targeting glioblastoma stem cells to overcome chemoresistance: an overview of current therapeutic strategies. Biomedicines *10*, 1308. https://doi.org/10.3390/biomedicines10061308.

26. Subramanian, A., Narayan, R., Corsello, S.M., Peck, D.D., Natoli, T.E., Lu, X., Gould, J., Davis, J.F., Tubelli, A.A., Asiedu, J.K., et al. (2017). A next generation connectivity Map: L1000 platform and the first 1, 000, 000 profiles. Cell *171*, 1437–1452.e17. https://doi.org/10.1016/j.cell.2017.10.049.

27. Wang, X., Bai, H., Zhang, X., Liu, J., Cao, P., Liao, N., Zhang, W., Wang, Z., and Hai, C. (2013). Inhibitory effect of oleanolic acid on hepatocellular carcinoma via ERK-p53-mediated cell cycle arrest and mitochondrial-dependent apoptosis. Carcinogenesis *34*, 1323–1330. https://doi.org/10.1093/carcin/bgt058.

28. Srivastava, S., and Chan, C. (2007). Hydrogen peroxide and hydroxyl radicals mediate palmitate-induced cytotoxicity to hepatoma cells: relation to mitochondrial permeability transition. Free Radic. Res. *41*, 38–49. https://doi.org/10.1080/10715760600943900.

29. Fisher, C.J., and Goswami, P.C. (2008). Mitochondria-targeted antioxidant enzyme activity regulates radioresistance in human pancreatic cancer cells. Cancer Biol. Ther. *7*, 1271–1279. https://doi.org/10.4161/cbt.7.8.6300.

30. Tamari, Y., Kashino, G., and Mori, H. (2017). Acquisition of radioresistance by IL-6 treatment is caused by suppression of oxidative stress derived from mitochondria after γ-irradiation. J. Radiat. Res. *58*, 412–420. https://doi.org/10.1093/jrr/rrw084.

31. Giovannoni, G. (2017). Cladribine to treat relapsing forms of multiple sclerosis. Neurotherapeutics *14*, 874–887. https://doi.org/10.1007/s13311-017-0573-4.

32. Deeks, E.D. (2018). Cladribine tablets: a Review in relapsing MS. CNS Drugs *32*, 785–796. https://doi.org/10.1007/s40263-018-0562-0.

33. Giovannoni, G., Soelberg Sorensen, P., Cook, S., Rammohan, K., Rieckmann, P., Comi, G., Dangond, F., Adeniji, A.K., and Vermersch, P. (2018). Safety and efficacy of cladribine tablets in patients with relapsing-remitting multiple sclerosis: results from the randomized extension trial of the CLARITY study. Mult. Scler. *24*, 1594–1604. https://doi.org/10.1177/1352458517727603.

34. Liliemark, J. (1997). The clinical pharmacokinetics of cladribine. Clin. Pharmacokinet. *32*, 120–131. https://doi.org/10.2165/00003088-199732020-00003.

35. Drokhlyansky, E., Smillie, C.S., Van Wittenberghe, N., Ericsson, M., Griffin, G.K., Eraslan, G., Dionne, D., Cuoco, M.S., Goder-Reiser, M.N., Sharova, T., et al. (2020). The human and mouse enteric nervous system at single-cell resolution. Cell *182*, 1606–1622.e23. https://doi.org/10.1016/j.cell.2020.08.003.

36. Miyai, M., Tomita, H., Soeda, A., Yano, H., Iwama, T., and Hara, A. (2017). Current trends in mouse models of glioblastoma. J. Neuro Oncol. *135*, 423–432. https://doi.org/10.1007/s11060-017-2626-2.

37. Bowman, R.L., Wang, Q., Carro, A., Verhaak, R.G.W., and Squatrito, M. (2017). GlioVis data portal for visualization and analysis of brain tumor expression datasets. Neuro Oncol. *19*, 139–141. https://doi.org/10.1093/neuonc/now247.

38. Chen, Y., and Wang, X. (2020). miRDB: an online database for prediction of functional microRNA targets. Nucleic Acids Res. *48*, D127–D131. https://doi.org/10.1093/nar/gkz757.

39. Sticht, C., De La Torre, C., Parveen, A., and Gretz, N. (2018). miRWalk: an online resource for prediction of microRNA binding sites. PLoS One *13*, e0206239. https://doi.org/10.1371/journal.pone.0206239.

40. McGeary, S.E., Lin, K.S., Shi, C.Y., Pham, T.M., Bisaria, N., Kelley, G.M., and Bartel, D.P. (2019). The biochemical basis of microRNA targeting efficacy. Science *366*, eaav1741. https://doi.org/10.1126/science.aav1741.

41. Lee, S., and Youn, B. (2020). Hypolipidemic roles of casein-derived peptides by regulation of trans-intestinal cholesterol excretion and bile acid synthesis. Nutrients *12*, 3058. https://doi.org/10.3390/nu12103058.

42. Lee, H., Shin, E., Kang, H., Youn, H., and Youn, B. (2021). Soybean-derived peptides attenuate hyperlipidemia by regulating trans-intestinal cholesterol excretion and bile acid synthesis. Nutrients *14*, 95. https://doi.org/10.3390/nu14010095.

43. Parker, C.G., Kuttruff, C.A., Galmozzi, A., Jørgensen, L., Yeh, C.H., Hermanson, D.J., Wang, Y., Artola, M., McKerrall, S.J., Josyln, C.M., et al. (2017). Chemical proteomics identifies SLC25A20 as a functional target of the ingenol class of actinic keratosis drugs. ACS Cent. Sci. *3*, 1276–1285. https://doi.org/10.1021/acscentsci.7b00420.

44. Pan, C., Jin, L., Wang, X., Li, Y., Chun, J., Boese, A.C., Li, D., Kang, H.B., Zhang, G., Zhou, L., et al. (2019). Inositol-triphosphate 3-kinase B confers cisplatin resistance by regulating NOX4-dependent redox balance. J. Clin. Invest. *129*, 2431–2445. https://doi.org/10.1172/jci124550.

45. Douglas, D.N., Pu, C.H., Lewis, J.T., Bhat, R., Anwar-Mohamed, A., Logan, M., Lund, G., Addison, W.R., Lehner, R., and Kneteman, N.M. (2016). Oxidative stress Attenuates lipid synthesis and increases mitochondrial fatty acid oxidation in hepatoma cells infected with hepatitis C virus. J. Biol. Chem. *291*, 1974–1990. https://doi.org/10.1074/jbc.M115.674861.

46. Kim, K., Lee, S., Kang, H., Shin, E., Kim, H.Y., Youn, H., and Youn, B. (2021). Dual specificity kinase DYRK3 promotes aggressiveness of glioblastoma by altering mitochondrial morphology and function. Int. J. Mol. Sci. *22*, 2982. https://doi.org/10.3390/ijms22062982.

47. Park, G., Son, B., Kang, J., Lee, S., Jeon, J., Kim, J.H., Yi, G.-R., Youn, H., Moon, C., Nam, S.Y., and Youn, B. (2019). LDR-induced miR-30a and miR-30b target the PAI-1 pathway to control adverse effects of NSCLC radiotherapy. Mol. Ther. *27*, 342–354. https://doi.org/10.1016/j.ymthe.2018.10.015.

STAR★METHODS

KEY RESOURCES TABLE

REAGENT or RESOURCE	SOURCE	IDENTIFIER
Antibodies		
DGKB, WB, dil: 1/1,000; IHC, dil: 1/150	Thermo Fisher Scientific	Cat# PA5-15416; RRID: AB_2091133
DGAT1, WB, dil: 1/1,000; IHC, dil: 1/150	Novus Biologicals	Cat# NB110-41487; RRID: AB_805567
α-tubulin, WB, dil: 1/2,000	Cell Signaling Technology	Cat# 2144S; RRID: AB_2210548
β-actin, WB, dil: 1/2,000	Cell Signaling Technology	Cat# 4967S; RRID: AB_330288
Cleaved caspase 3 (Asp175), WB, dil: 1/1,000; IHC, dil: 1/150	Cell Signaling Technology	Cat# 9661S; RRID: AB_2341188
Cleaved caspase 9 (Asp330), WB, dil: 1/1,000	Invitrogen	Cat# PA5-77889; RRID: AB_2735576
Cleaved PARP, WB, dil: 1/1,000	Cell Signaling Technology	clone 46D11, Cat# 9532S; RRID: AB_659884
Cytochrome C, WB, dil: 1/1,000	BD Biosciences	clone 7H8.2C12, Cat# 556433; RRID: AB_396417
COX IV (3E11), WB, dil: 1/1,000	Cell Signaling Technology	Cat# 4850S; RRID: AB_2085424
Annexin V, Flow Cytometry, dil: 1/100	Invitrogen	Cat# PA5-27872; RRID: AB_2545348
Anti-mouse IgG, HRP-linked Antibody, WB, dil:1/5,000 - 10,000	Thermo Fisher Scientific	Cat# 31430; RRID: AB_228307
Anti-rabbit IgG, HRP-linked Antibody, WB, dil:1/5,000 - 10,000	Thermo Fisher Scientific	Cat# 31460; RRID: AB_228341
Chemicals, peptides, and recombinant proteins		
RNeasy Plus Kits	Qiagen	74034
Trans-Dux virus transduction reagent(200x)	System Biosciences	LV850A-1
PEG-it Virus Precipitation Solution	System Biosciences	LV810A-1
Ultra-Rapid Lentiviral Global Titering Kit	System Biosciences	LV961A-1
Dulbecco's Modified Eagle's Medium (DMEM)	WELGENE Inc.	LM 001-05
DMEM/F-12	WELGENE Inc.	LM 002-08
Dulbecco's Phosphate-Buffered Saline (D-PBS)	WELGENE Inc.	LB 001-02
EGF, Epidermal Growth Factor human	Gibco	PHG0311
FGF, Fibroblast Growth Factor	Gibco	PHG0261
B-27 Supplement (50X), minus vitamin A	Gibco	12587010
TRIzol Reagent	meridian BIOSCIENCE	BIO-38032
SensiFAST SYBR Hi-ROX Kit	Bioline	92020
RIPA Lysis and Extraction Buffer	Thermo Fisher Scientific	89900
Bio-Rad Protein Assay Kit II	BIORAD	5000002
10x Tris/Tricine/SDS Running Buffer	BIORAD	1610744
Bovine serum albumin (BSA)	MP Biomedicals	160069
TBS	TransLab	TLP-118.3
Tween 20	Thermo Fisher Scientific	J20605-AP
Triton X-100	Sigma-Aldrich	X100
Nitrocellulose Membrane	MERCK	GE10600002
ECL Western Blotting Detection Reagents	Thermo Fisher Scientific	34580
CellTiter-Glo® Luminescent Viability Assay kit	Promega	G7570
Crystal violet	Sigma-Aldrich	C0775
Isoflurane	Hana Pharm	N/A
VivoGlo™ Luciferin, *In Vivo* Grade	Promega	P1041
Paraformaldehyde solution	Thermo Fisher Scientific	J19943-K2
Xylene	DaeJung	8587-4404
Hematoxylin	TissuePro	H08-500R
Eosin Y	TissuePro	EY07-500R

Continued

REAGENT or RESOURCE	SOURCE	IDENTIFIER
Hydrochloric acid	Duksan	1129
Hydrogen peroxide	DaeJung	4104-4405
Protein Block Serum-Free	Dako	X0909
Antibody Diluent, Background Reducing	Dako	S302281-2
EnVision + Single Reagent (HRP. Mouse)	Dako	K4001
EnVision + Single Reagent (HRP. Rabbit)	Dako	K4003
Liquid DAB + Substrate Chromogen System	Dako	K3468
DAG Kinase Activity Assay Kit	CELL BIOLABS	MET-5036
Diacylglycerol Assay Kit	Abcam	ab242293
Phosphatidic Acid Assay Kit	Abcam	ab273335
ATP Assay Kit	Abcam	ab83355
L-carnitine	Tokyo Chemical Industry	C0049-25G
Triglyceride Assay Kit	Abcam	ab65336
Laminin	Sigma-Aldrich	CC095
BODIPY	Thermo Fisher Scientific	D3922
Hoechst	MERCK	14533
Anti-Fade Fluorescence Mounting Medium - Aqueous,Fluoroshield	Abcam	ab104135
Rhodamine 123	Thermo Fisher Scientific	R302
MitoSOX Red Mitochondrial Superoxide Indicator, for live-cell imaging	Invitrogen	M36008
MitoPY1	Tocris	4428
Cladribine	Tokyo Chemical Industry	C2499
Temozolomide	Tokyo Chemical Industry	T2744
N-Acetyl-L-cysteine	Sigma-Aldrich	Cat#A7250
Deposited data		
RNA-seq data	This study	GEO: GSE207002
Experimental models: Cell lines		
Human GBM cell: U87MG	Korea Cell Line Bank	Cat#30014
Human GBM cell: A172	Korea Cell Line Bank	Cat#21620
Human hepatocellular carcinoma cell: HepG2	Korea Cell Line Bank	Cat#88065
Human pancreatic carcinoma cell: MIA-PaCa2	Korea Cell Line Bank	Cat#21420
Human pancreatic adenocarcinoma cell: AsPc-1	Korea Cell Line Bank	Cat#21682
Human gallbladder carcinoma cell: SNU-308	Korea Cell Line Bank	Cat#00308
Human lung adenocarcinoma cell: A549	Korea Cell Line Bank	Cat#10185
Human lung carcinoma cell: NCI-H292	Korea Cell Line Bank	Cat#21848
Human monocyte: THP-1	Korea Cell Line Bank	Cat#40202
Human glioblastoma stem cell: BCL20-HP02	Patient derived	Table S1
Human glioblastoma stem cell: BCL21-HP03	Patient derived	Table S1
Human glioblastoma stem cell: GSC11	Dr. Frederick F. Lang	N/A
Experimental models: Organisms/strains		
Athymic nude mice	OrientBio	N/A
Oligonucleotides		
Primers for qRT-PCR	Macrogen	Table S2
Recombinant DNA		
pLKO vector	Addgene	8453
Control shRNA	Sigma-Aldrich	SHC201
shDGKB (Target sequence: CCTAATGACAAAGATGAGAAA)	Sigma-Aldrich	TRCN0000000765

(Continued on next page)

Continued

REAGENT or RESOURCE	SOURCE	IDENTIFIER
shDGAT1 (Target sequence: ACTACTACGTGCTCAACTATG)	Sigma-Aldrich	TRCN0000236203
psPAX2	Addgene	12260
pMD2.G	Addgene	12259
Software and algorithms		
ZEN 3.4 (blue edition)	Zeiss	https://www.zeiss.com/microscopy/us/downloads.html
StepOne Software	Applied Biosystems	https://www.thermofisher.com/kr/en/home/technical-resources/software-downloads/StepOne-and-StepOnePlus-Real-Time-PCR-System.html
Seahorse Wave Controller	Agilent	https://www.agilent.com/
GraphPad Prism 9	GraphPad	https://www.graphpad.com/scientificsoftware/prism/
GlioVis	Bowmanet al.[37]	http://gliovis.bioinfo.cnio.es/
miRDB	Chen, et al.[38]	https://mirdb.org/
miRWalk	Sticht et al.[39]	http://mirwalk.umm.uni-heidelberg.de/
TargetScan	McGeary et al.[40]	https://www.targetscan.org/vert_80/
R	R Core	https://www.R-project.org/
Original code	This study	Data S1
Other		
TrueBeam STx	Varian Medical Systems	N/A
VISQUE Invivo Smart LF	Vieworks	N/A

RESOURCE AVAILABILITY

Lead contact
Further information and requests for resources and reagents should be directed to and will be fulfilled by the lead contact, Dr. BuHyun Youn (bhyoun72@pusan.ac.kr).

Materials availability
This study did not generate new reagents.

Data and code availability
- RNA sequencing data has been deposited at NIH Gene Expression Omnibus (GEO): GSE207002 and are publicly available as of the date of publication.
- All original code is available in this paper's supplemental information Data S1.
- Any additional information required to reanalyze the data reported in this work paper is available from the lead contact upon request.

EXPERIMENTAL MODEL AND SUBJECT DETAILS

Glioblastoma stem cell derivation
Patient-derived GSC11 glioblastoma stem cells were provided by Dr. Frederick F. Lang (Department of Neurosurgery, The University of Texas, M. D. Anderson Cancer Center, Houston, USA); patient-derived BCL20-HP02 and BCL21-HP03 glioblastoma stem cells were obtained from patients undergoing resection in accordance with a protocol approved by Haeundae Paik Hospital (Inje University, Busan, Republic of Korea). BCL20-HP02 GSCs were derived from a GBM from a 38-year old male patient. BCL21-HP03 GSCs were derived from a GBM from a 67-year old male patient. Detailed information of the patients is summarized in Table S1. More specifically, after the resection, about 200–500 mg of tumor samples were collected into a tube containing DMEM/F-12 supplemented with B27 without vitamin A. Tumor specimen was then washed with 5 mL of HBSS to remove blood and debris. After the washing, the tumor was cut into small fragments and minced with a sterile scalpel blade into approximately 1 mm³ fragment. To dissociate GBM tumor tissue, the minced tumor was treated with collagenase D (1 mg/mL) and DNase I (0.1 mg/mL) in HBSS and incubated at 37°C for 30 to 90 min with gentle mixing. Finally, the solution was passed through the 70 μm sterile mesh filter

to remove any large, undigested tumor pieces. To culture cells as tumorspheres, the patient-derived glioblastoma stem cells were cultured in DMEM/F-12 supplemented with B27, EGF (20 ng/mL), bFGF (20 ng/mL), penicillin/streptomycin (10,000 U/ml) at 37°C in a humidified atmosphere of 95% air and 5% CO_2. For adherent cell cultures, the cells were plated in laminin-coated plate in the same medium composition.

Establishment of radioresistant cells

To acquire radioresistant GBM cells, *in vivo* selection was processed 3 times in total. First, 2×10^6 U87MG cells-expressing luciferase were subcutaneously implanted in six-week-old male BALB/c athymic nude mice and exposed to IR (2 Gy/day for 5 days, F1). Implanted U87MG cells were monitored once a week by mouse bioluminescence imaging until 35 days after IR. Then, implanted U87MG cells were extracted from F1 mice and cultured in DMEM with 10% FBS and 1% antibiotics. Next, 2×10^6 F1-derived U87MG cells were subcutaneously implanted in six-week-old male BALB/c athymic nude mice and exposed to IR (2 Gy/day for 5 days, F2). Like U87MG cells of the F1 mouse, cells were monitored once a week by mouse bioluminescence imaging until the mice were dead. Then, implanted U87MG cells were extracted from F2 mice and cultured in DMEM with 10% FBS and 1% antibiotics. Lastly, 5×10^5 F2-derived U87MG cells were orthotopically implanted in six-week-old male BALB/c athymic nude mice and exposed to IR (2 Gy/day for 5 days). Cells were monitored once a week by mouse bioluminescence imaging until the mice were dead. Then, implanted U87MG cells were extracted from mice, cultured in DMEM with 10% FBS and 1% antibiotics, and referred to as U87MG-RR. Additionally, U87MG-RR cells were validated by being compared with parental U87MG cells in xenograft, tissue imaging, stemness marker, and limited dilution assay.

Animal care protocol and orthotopic xenograft mouse model

Six-week-old male BALB/c athymic nude mice were used for generating xenograft mouse model following the previous study.[4] All experiments were performed in accordance with the provisions of the NIH Guide for the Care and Use of Laboratory Animals. The mice were housed individually or in groups of up to five in sterile cages, and were maintained in animal care facilities in a temperature regulated room (23 ± 1°C) with a 12 h light–dark cycle. All animals were fed water and standard mouse chow *ad libitum*. U87MG-RR-luciferase expressing cells and HP03-luciferase expressing cells were harvested and suspended at a density of 1×10^5 cells per μL in serum free media. Then, 5×10^5 cells were injected into the mice brains using 10 μL syringe with stereotactic surgery. 7 days after the injection, the brain of injected mice were irradiated with 2 Gy daily for five days at a dose rate of 600 MU/min using a TrueBeam STx. Xenograft growth was monitored by bioluminescent imaging using VISQUE *Invivo* Smart LF. Mice were sacrificed upon manifestation of neurological symptoms.

Cell lines, cell culture, and irradiation

U87MG, A172, and HepG2 cell lines were obtained from the Korea Cell Line Bank (KCLB, Seoul, Republic of Korea). The phenotypes of these cell lines have been authenticated by the KCLB. All cells were free of mycoplasma contamination and were authenticated by short tandem repeat profiling within the past 12 months. U87MG-luciferase expressing cells were transferred via a material transfer agreement from Severance Hospital (Yonsei University, Seoul, Republic of Korea). The cells were grown in DMEM supplemented with 10% FBS, penicillin (100 U/ml), and streptomycin (100 mg/mL) at 37°C in a humidified atmosphere of 95% air and 5% CO_2. The cells were exposed to a single dose of X-ray using an X-ray generator M-150WE at a dose rate of 0.38 Gy/min. The radiation was delivered by using an 8 mm-diameter collimator.

METHOD DETAILS

RNA-sequencing

To obtain RNA samples from U87MG and U87MG-RR, U87MG and U87MG-RR cell lines were incubated upon 1×10^6 cells. RNA samples from U87MG and U87MG-RR were obtained through RNA extraction kit and 3 biological samples of each cell lines were prepared. RNA sequencing was performed through Illumina sequencing platform by ebiogen (Seoul, Republic of Korea). All RNA sequencing results of samples were assessed by triplicate. For quantifications, Fisher exact test was used for comparing U87MG and U87MG-RR groups. Genes were classified depend on significancy ($p < 0.05$) and fold change (>1.8 or <0.55).

Analysis of GBM poor prognosis-related genes

To obtain GBM poor prognosis-related gene, we utilized the list of gene expression in GBM patients through R language. First, we installed and utilized the packages, including 'ggplot2', 'dplyr', 'TCGAbiolinks', 'GEOquery', 'SummarizeExperiment', 'biomaRt', 'stringr', and 'tidyverse' on R system. Next, we performed 'TCGAbiolinks' and downloaded TCGA-GBM cohort. Then, the data was queried by 'GEOquery' as data category, data type, sample type, experimental strategy, and workflow type. We performed the gene naming and tubulin normalization. Because our focus of TCGA-GBM cohort is poor prognosis in primary tumor, we extracted clinical data through specifying data category is 'clinical' and sample type is 'primary tumor'. Next, to obtain the information of prognosis, we arranged the data as days to death and divided as quartile (top 25% or bottom 25%) or half (top 50% or bottom 50%). Finally, we selected statistically significant genes (both quartile p value <0.05 and half p value <0.05). The codes for analyzing GBM poor prognosis-related genes have been uploaded as supplemental information (Related to Data S1).

Quantitative real-time PCR

For mRNA expression assessment, qRT-PCR was performed following the previous study.[41] Briefly, RNA was isolated with TRIzol following the manufacturers' instructions and real-time qRT-PCR was performed using an Applied Biosystems StepOne Real-Time PCR System. It was performed for 40 cycles of 95°C for 15 s and 60°C for 1 min followed by thermal denaturation. The expression of each gene relative to GAPDH mRNA was determined using the $2^{-\Delta\Delta Ct}$ method. The sequences of the primers used are listed in Table S2. Each sample was assessed by triplication.

Western blots

The protein expression was validated as previously described.[42] Briefly, whole cell lysates (WCL) were prepared using radioimmunoprecipitation assay (RIPA) lysis buffer (50 mM Tris, pH 7.4, 150 mM NaCl, 1% Triton X-100, 25 mM NaF, 1 mM dithiothreitol, and 20 mM ethylene glycol tetraacetic acid supplemented with protease inhibitors) and the protein concentrations were determined using a BioRad protein assay kit (BioRad Laboratories, Hercules, CA, USA). Protein samples were subjected to SDS-PAGE, transferred to a nitrocellulose membrane and then blocked with 5% BSA in tris-buffered saline with Tween 20 (10 mM Tris, 100 mM NaCl, and 0.1% Tween 20). The membranes then were probed using the specific primary antibodies and peroxidase-conjugated secondary antibodies from Thermo Fisher Scientific. For all western immunoblot experiments, blots were imaged using an ECL detection system (Roche Applied Science, Indianapolis, IN, USA) with iBright FL1000 Imaging System from Thermo Fisher Scientific.

Lentiviral transduction

HEK-293 cells were seeded at 1×10^6 cells with DMEM with FBS in 150mm plates 1 day before lentiviral transfection. When cell confluency was approximately 50%, transfection mixture, Opti-MEM with pLKO.1, psPAX2, and pMD2.G, was added through TransIT-LT1 reagent agent. After 18 h, media was exchanged to DMEM with FBS and antibiotics. Then, 6 h later, media was harvested and centrifuged at 1,500 g for 15 min. After centrifugation, supernatant was transferred other fresh tube and Virus Precipitation Solution was added to tube and incubated at 4°C for 12 h. To obtain lentiviral particles, supernatant with solution was centrifugated at 1,500 g for 5 min, and the pellet was diluted at 1/10-1/100 with PBS. The virus titer was quantified by real-time PCR by using Ultra-Rapid Lentiviral Global Titering Kit. For lentiviral transduction, target cells were seeded at appropriate plates and incubated up to 50 to 70% confluency. Then, transduction solution, culture medium combined with Trans-Dux to a 1X final concentration, was added to cells as for the desired MOI. 3 days after transduction, cells were selected by puromycin.

Cell viability assay and colony-forming assay

For cell viability assay, cells were seeded at 10,000 cells per well in 96-well plates 1 day before IR, or IR combined with DGKB shRNA transfection or DGKB plasmid transfection or DGKB mutant transfection for 48 h. Cell viability was determined using CellTiter-Glo Luminescent Viability Assay kit. Colony-forming assay was performed following the previous study.[5] Briefly, the cells were seeded at a density of 600 cells in 35-mm culture dishes. After 24 h, the cells were treated with IR, or IR combined with DGKB knockdown or overexpression. 14 days after seeding, the cells were fixed with 10% methanol and 10% acetic acid, which were then stained with 1% crystal violet. Colonies containing more than 50 cells were identified using densitometry software and scored as survivors.

Mouse bioluminescence imaging

Mice implanted with U87MG-RR and BCL21-HP03 cells expressing luciferase were injected intraperitoneally with a Luciferin solution (3 mg/mL in PBS, dose of 15 mg/kg) by an intraperitoneal route. After 10 min, mice were anesthetized by inhalational way using isoflurane and bioluminescence images were acquired using VISQUE *Invivo* Smart LF.

Hematoxylin and Eosin (H&E) and Immunohistochemistry (IHC) staining

H&E staining and IHC were performed as previously described.[5] The brain samples were embedded in paraffin blocks, and the sections were prepared by HistoCore AutoCut. Next, the sections were cut into 4 μm sections and stained with H&E, following standard procedures. For IHC, sections were treated with 3% hydrogen peroxide/methanol and then with 0.25% pepsin to retrieve antigens. Next, samples were incubated in blocking solution, after which they were incubated at 4°C overnight with the specific primary antibodies diluted in the antibody diluent. The sections were subsequently washed with tris-buffered saline with 0.1% Tween 20 and then incubated with polymer-horseradish peroxidase conjugated secondary antibody. A 3,3′-diaminobenzidine substrate chromogen system was utilized to detect antibody binding. Stained sections were observed under an Olympus IX71 inverted microscope. The quantification of IHC was processed by ImageJ. IHC images were loaded into ImageJ, and a color threshold was adjusted. To measure the total area, the hue and saturation values were adjusted to the maximum, the brightness was adjusted to the point where all tissues were selected, and the selected area (total area) was measured. To measure the IHC stained area, the selected area (IHC stained area) was measured by adjusting the color value until only the IHC stained area was selected without changing the brightness. To calculate the IHC stained area, the IHC stained area value was divided by the total area value and multiplied by 100.

Enzyme activity assay

For DGKB enzymatic activity quantification, cells were seeded at 10,000 cells per well in 96-well plates 1 day before IR, or IR combined with DGKB mutant for 48 h. DGKB activity were assessed by DAG kinase Activity Assay Kit following the manufacturers'

instructions. In detail, DAG substrate and kinase buffer was added to wells. Then control and treated samples were added to same wells and mix thoroughly following incubation for 30 min at 37°C. Next, the mixture was transferred to black 96-well plate and lipase solution is added following incubation for 30 min at 37°C. Finally, detection enzyme mixture is added to wells and incubated room temperature for 10 min in dark. Then, the plate was read by a GloMax Discover Microplate Reader equipped for excitation in the 530-560 nm range and for emission in the 585-595 nm range.

LC-MS/MS lipid profiling

Lipid profiling were performed as previously reported.[43] Cells were seeded in 10 cm plates 1 day before IR, or IR combined with DGKB shRNA transfection or DGKB plasmid transfection or miR-3918 mimic transfection for 48 h. When cells were 90% confluency, media were removed and cells were washed carefully with PBS and resuspended in serum-free media. After incubation at 37°C for 3 h, the media was removed and cells were washed with PBS. Cells were scraped in PBS, transferred to a fresh tube and centrifuged at 2,000 rpm for 8 min, and resuspended in PBS. Then, cells were lysed using a sonicator, and 1 mL of lysates normalized to 1.5 mg/mL was transferred to 2-dram glass vials. Internal standard mix was added to lysates and vigorously vortexed. Samples were centrifugated at 1,000 rpm for 5 min to pellet insoluble precipitate, and the remaining eluent carefully transferred to fresh 2-dram vials. Samples were reconstituted in 500 μL of mixture (lipid species:H_2O, 1:1 vol/vol) and analyzed by LC/MS/MS. The indicated lipid species were quantified by measuring the area under the peak relative to an internal standard.

Metabolic assays

DAG, PA, TG, and ATP levels were assessed by utilizing fluorometric assay kits (DAG, ab242293; PA, ab273335; TG, ab65336; ATP, ab83355) following the manufacturers' instructions. Briefly, cells were seeded at 10,000 cells per well in 96-well plates 1 day before IR, or IR combined with transfection (shDGKB, shDGAT1, and DGKB) or treatment (DAG, PA, miR-3918 mimic, and cladribine) for 48 h. DAG and PA were kept as 1000-fold concentrated stock solutions in chloroform, dried prior to use under N_2 stream, and emulsified by sonication for 10 min in 150 mM NaCl, 10 mM Tris-HCl, pH 8.0. DAG and PA in vesicles were added to cells to a final concentration of 50 μM. Then, appropriate buffer is added to sample-loaded wells and plates were incubated by fit for the situation. Finally, the plates were read by a GloMax Discover Microplate Reader equipped for contextual excitation/emission fluorescence filter. Glycolytic rate, lipid synthesis, and RNA synthesis were assessed as previously described.[44] Glycolytic rate was determined by measurement of ^3H_2O release. In brief, cells were spiked with 20 μCi/mL of D-[U-^{3}H]glucose in Krebs buffer supplemented with 10 mM glucose for 1 h. Diffused ^3H_2O from D-[U-^{3}H]glucose was measured by liquid scintillation counting, and values were normalized with cell numbers of each sample. For lipid synthesis, lipids were extracted using solvent of hexane and isopropanol (3:2 v/v). The solvent was air-dried and resuspended in chloroform. The amount of ^{14}C-lipid was determined by liquid scintillation counting and normalized to the amount of protein. For RNA synthesis, subconfluent cells were spiked with 4 μCi/mL of D-[U-^{14}C]glucose for 2 h. Total RNA was extracted, and the labeled RNA was quantified by liquid scintillation counting and normalized to the total RNA amount.

Fatty acid oxidation

These experimental conditions were adapted from studies conducted by Hansson et al.[45] Cells were seeded in 60-mm culture dishes and allowed to adhere for 4 h prior to pulse labeling for 4 h with 2 mL of serum-free DMEM containing 5 μCi of [9,10-^{3}H] oleic acid (0.4 mM oleic acid complexed to 0.4% BSA) to stimulate neutral lipid synthesis. After 4 h, the pulse media were removed by aspiration and retained for analysis, and cells were washed three times with serum-free DMEM containing 0.4% fatty acid-free BSA. Then, cells were incubated with 2 mL of serum-free DMEM for an additional 4 h (chase) prior to collecting the chase media for analysis. Pulse and chase media samples were centrifuged at 2,500 g for 5 min to remove cell debris. Labeled fatty acids were precipitated out from media samples by the addition of 30 μL of 20% BSA and 16 μL of 70% perchloric to 200 μL of culture media. Media were then centrifuged at 25,000 g for 5 min before an aliquot of the supernatant was counted for radioactivity. The cells were washed with ice-cold PBS, and cell homogenates were prepared in the same buffer, and protein concentration was measured. Lastly, the amount of radioactivity in lysates was determined by scintillation counting.

Seahorse analysis

Oxygen consumption rate (OCR) and extracellular acidification rate (ECAR) were measured by Seahorse XFe24 Extracellular Flux Bioanalyzer (Agilent Technologies) with 80–90% confluent cells following the previous study.[5] Briefly, 10,000 cells were seeded in 24-well Seahorse plate. In the next day, cells were treated with IR or IR combined with DGKB shRNA transfection or DGKB plasmid transfection. 24 h later, cells were equilibrated for 1 h in a non-CO_2 incubator. For the OCR assay, the media were changed to the FAO assay buffer (Agilent Technologies). Injection port A on the sensor cartridge was loaded with oligomycin (2 μM), port B was loaded with FCCP (1 μM), and port C was loaded with rotenone/antimycin A (1 μM each). For the ECAR assay, the media were changed to the FAO assay buffer (Agilent Technologies) without glucose. The injection port A was loaded with glucose (10 mM), port B was loaded with oligomycin (2 μM), and port C was loaded with 2-Deoxy-D-glucose (100mM). A minimum of three wells were utilized per condition to calculate OCR and ECAR.

Lipid droplet staining and quantification

For live cells, LDs were stained with BODIPY 493/503 (0.5 mM) for 30 min and visualized by confocal microscopy (Carl Zeiss LSM800, 63x/1.4 NA oil). More than 30 cells were analyzed and LDs were quantified by ImageJ, as previously described.[13] In xenograft tumor tissues, we utilized immunofluorescence using TIP47 antibody. After antigen retrieval, sections were incubated with the TIP47 antibody, followed by incubation with an appropriate secondary antibody, and slides were then mounted, imaged, and LD counted by using ImageJ.

Mitochondrial membrane potential

4 days before imaging, cells were seeded at 10,000 cells on confocal plate. In the next day, cells were treated with IR or IR combined with DGKB shRNA transfection or DGKB plasmid transfection. 72 h later, cells were washed for 3 times with PBS. Then, cells were placed in FluoroBrite DMEM with 5% FBS and Rhodamine 123 (0.05 mg/mL) for 30 min. Additionally, cells were washed for twice with PBS and incubated with Hoechst 33342 for 30min. Finally, cells were visualized by confocal microscopy (Carl Zeiss LSM800, 63x/1.4 NA oil). A minimum of 100 cells were analyzed and fluorescence was quantified with ImageJ.

Transmission Electronic microscopy (TEM)

TEM imaging was performed as previously described.[46] Briefly, the material was pre-fixed with 2.5% glutaraldehyde in PBS (pH 7.2) at 4°C and was post-fixed with 1% osmium tetroxide in PBS. The material was dehydrated with a series of the graded ethyl alcohol, and embedded in epoxy resin (Epon 812 mixture). Sections (70 nm) were produced on an ultramicrotome (EM UC7) and were double stained with uranyl acetate and lead citrate. The sections were then analyzed with a transmission electron microscope (JEM-1200EXII). This experiment was performed at Pusan National University Hospital.

Reactive oxygen species detection

After washing cells 3 times with PBS, cells were placed into FluoroBrite DMEM with 5% FBS supplemented and 0.5 μM MitoSOX Red Mitochondrial Superoxide Indicator and incubated for 10 min at 37°C. After washing twice with PBS, cells were then incubated with Hoechst33342 for 30 min before confocal imaging. A minimum of 100 cells were analyzed and fluorescence was quantified by the ImageJ.

Mitochondria and cytosol fractionation

The mitochondrial proteins were prepared using Mitochondria/Cytosol Fractionation Kit following the manufacturer's instructions. Briefly, cells were harvested and washed with PBS, and resuspended with Lysis buffer and incubated at 4°C for 10 min. The cells were centrifuged at 1,000 g at 4°C for 10 min, and the supernatants were used as the cytosolic fractions. Pellets were resuspended in Disruption buffer and disrupted by using a 21G needle and a syringe. Following a centrifugation at 1,000 g at 4°C for 10 min, the supernatants were transferred to new tubes and centrifuged at 6,000 g at 4°C for 10 min. The pellets containing mitochondria were resuspended in Mitochondria storage buffer, and centrifuged at 6,000 g at 4°C for 20 min. Pellets were then resuspended in Mitochondria storage buffer and protein concentration was determined.

Apoptosis assay (Annexin V/PI)

The Annexin V-fluorescein isothiocyanate (FITC) kit was used to detect apoptosis as previously described.[47] Following DGKB or DGAT1 shRNA transfection or DGKB plasmid transfection, cells (10^5-10^6 cells/mL) were harvested, washed with ice-cold PBS, and resuspended in 100 mL of ice-cold 1X binding buffer. Next, 25 ng of Annexin V-FITC and 250 ng of PI were added to the cell suspension and the cells were incubated on ice for 10 min in the dark. Finally, the stained cells were diluted to a final volume of 250 mL with binding buffer and analyzed using a FACS Verse flow cytometer.

Luciferase reporter gene assay

Genomic region harboring the DGAT1 promoter (−1000 to +226 bp of the transcription start site of the gene) was cloned into pGL3-NFAT luciferase vector digested by MluI and HindIII. A luciferase assay was performed as previously reported.[47] Briefly, luciferase activity was measured using Luciferase Assay System from Promega. Cells were seeded in 60mm culture dishes 1 day before transfection and irradiation. At 48 h after transfection, media was removed and the dishes were washed by PBS. 400 μL of Cell Culture Lysis Reagent was added to the dishes directly and transferred to new tubes. After brief centrifugation, 20 μL of cell lysate was mixed with 100 μL of Luciferase Assay Reagent. Luminescence was measured using a GloMax Discover Microplate Reader.

Intracerebral injection procedures

For intracerebral administration of lentivirus vectors, mice were first anesthetized by inhalation of 1–3% isoflurane in oxygen and positioned in a stereotaxic frame. Viral supernatant injections (1 μL per injection; viral supernatant concentrations ranged from 5.5×10^8 to 4.5×10^9 infectious units (IFU) per mL) were delivered into the mice brains using 10 μL syringe with stereotactic surgery. Injection sites, the same site of xenograft, were according to the following stereotaxic position: at stereotactic coordinates of bregma, −1 mm anteroposterior, and +2 mm mediolateral using stereotaxic injection frame. To deliver the virus, a small hole was drilled through the skull, and a microliter syringe was lowered to injection site. The viral supernatant injection was delivered over 60 s. After

the infusion, the syringe was left in place for a further 60 s. The syringe then raised to the next more dorsal injection site, and the injection procedure repeated. After the final virus supernatant injection, the drill holes in the skull were filled with bone wax, the scalp sutured and the incision site treated with antibiotic ointment.

QUANTIFICATION AND STATISTICAL ANALYSIS

All numerical data are presented as the means ± SEM from at least three independent experiments. For quantifications, two-tail unpaired Student's *t* test was used for comparing two experimental groups, and one-way ANOVA with appropriate post-hoc test was applied when needed to compare three or more experimental groups. Log rank (Mantel-Cox) test was used for statistical analysis of survival. The Prism 9 software was used for all statistical analyses. A p value <0.05 was considered to be statistically significant.